Evaluation of the representation of raindrop self-collection and breakup in two-moment bulk models using a multifrequency radar retrieval

Laurence Niquet, Frédéric Tridon, Pierre Grzegorczyk, Antoine Causse, Baptiste Bordet, Wolfram Wobrock, Céline Planche

Evaluation of the representation of raindrop self-collection and breakup in two-moment bulk models using a multifrequency radar retrieval

Laurence Niquet[1], Frédéric Tridon[2,1], Pierre Grzegorczyk[1], Antoine Causse[1], Baptiste Bordet[3], Wolfram Wobrock[1], and Céline Planche[1,4]

[1]Université Clermont Auvergne, CNRS INSU, Laboratoire de Météorologie Physique UMR 6016, F-63000 Clermont-Ferrand, France.

[2]DIATI, Politecnico di Torino, Turin, Italy.

[3]Université Grenoble Alpes, Laboratoire Interdisciplinaire de physique UMR 5588, F-38000 Grenoble, France.

[4]Institut Universitaire de France (IUF).

Corresponding authors: Céline Planche (celine.planche@uca.fr) and Frédéric Tridon (frederic.tridon@polito.it)

Key Points:

- The temporal variation of raindrop concentrations as they fall is derived from zenith pointing Ka- and W-band radar measurements.
- Raindrop concentration rate obtained from the parameterizations of microphysical processes used in mesoscale models differ from observations.
- A new parameterization of self-collection and breakup processes based on the multifrequency radar observations is proposed.

Plain Language Summary

A better knowledge of atmospheric processes leading to precipitation is mandatory to better predict severe floods and mitigate their impact on human societies, in particular in the context of climate change. Some of the most uncertain rain microphysics processes are the raindrop self-collection and breakup. These processes are represented in numerical weather prediction (NWP) models via significantly different parameterizations, based on few laboratory experiments or from purely empirical approaches. In this work, two types of precipitating systems are studied, a frontal situation that occurred over Finland in June 2014 and a squall line system observed over Oklahoma in June 2011. In both cases, multifrequency radar observations provide raindrop size distribution (RSD) with high spatial and temporal resolution. Comparisons between observations and current parameterizations show significant divergences. Hence, a new parameterization of raindrop self-collection and breakup processes is developed based on multifrequency radar observations.

Abstract

Using multifrequency radar observations providing raindrop size distribution (RSD) evolution with high spatial and temporal resolution, this study aims to assess the ability of different parameterizations of raindrop self-collection and breakup processes applied in mesoscale models, to reproduce the statistics derived from observations. The stratiform zones of two types of precipitating systems are studied, a frontal situation that occurred over Finland in June 2014 and a squall line system observed over Oklahoma in June 2011. An analysis method for determining raindrop trajectories was used to obtain the temporal variation of the total raindrop concentration from the observations. The resulting raindrop concentration rate as a function of the mean volume diameter reveals significant differences with the parameterizations currently used in two-moment bulk microphysics schemes. These results show that even if they produce variations in raindrop concentration of the same order of magnitude as the observations, the current parameterizations diverge from the median of the observations, resulting in an overestimation of either the self-collection or the breakup process. From the median of radar observations, new parameterizations of the self-collection and breakup processes and of rain self-collection efficiency are developed and can be implemented in two-moment bulk microphysics schemes.

1 Introduction

Over the last decades, floods have been one of the types of disaster causing the most material damage and fatalities. To improve the forecast of extreme rain events, precipitation and the associated microphysical processes need to be better represented in forecasting models. In previous studies, it was shown that microphysical processes of rain, and in particular raindrop collection (i.e. collision-coalescence) and breakup (collisional breakup), can have an impact not only on surface precipitation rate but also on the dynamics of precipitating systems (Morrison & Milbrandt, 2011; Morrison et al., 2012; van Weverberg et al., 2012) and on the ice formation in convective systems (Seifert et al., 2005). In the literature, the term collection can refer to different processes (Seifert & Beheng, 2006; Khain et al., 2015): autoconversion when considering collection between cloud droplets which results in raindrops, accretion when considering the collection of cloud droplets by raindrops leading to the growth of the raindrops and self-collection when considering the collection between hydrometeors of the same type. In this work, we focus on the collection between raindrops only, i.e the raindrop self-collection process.

In order to investigate the behavior of raindrop interactions, laboratory experiments have been carried out to study the effect of collision/coalescence (List & Whelpdale, 1969; List et al., 1970, and others) and breakup (McTaggart-Cowan & List, 1975; Low & List, 1982a; Szakall & Urbich, 2018). From their collisions experiments, Low & List (1982a, 1982b) defined a breakup parameterization which is still commonly used even if the effect of size was investigated by using only 10 pairs of raindrops. These few laboratory experiments are at the base of the raindrop coalescence/breakup efficiencies that are used in bin and Lagrangian microphysics schemes such as in the Hebrew University Cloud Model (HUCM) (Khain et al., 2004; Seifert et al., 2005), in the Detailed SCAvenging Model (DESCAM) (Flossmann & Wobrock, 2010; Planche et al., 2010, 2014) and in other models (see references in Khain et al., 2015). Similarly, in two-moment bulk models, current parameterizations of self-collection and breakup processes (as in Ziegler, 1985) are based on the stochastic collection equation (Berry, 1967; Berry & Reinhardt, 1974) and on the collection kernels defined by Long (1974). Hence, this topic would clearly benefit from newer and more complete experiments which would allow to understand the behavior of colliding raindrops

of various sizes, as it was recently done for the study of ice collisional breakup (Grzegorczyk et al., 2023).

Despite the continuous development of cloud models over the last decades, it is still a challenge to represent raindrop self-collection and breakup in bin and bulk models (Morrison et al., 2020). While comparisons between modeling results and observations are usually performed by exploiting ground-based disdrometers (Kagkara et al., 2020; Saleeby et al., 2022), observations of the profile of the raindrop size distribution (RSD) are needed to make a significant progress (Morrison et al., 2020). For example, recent studies by Tridon et al. (2019b) and Planche et al. (2019) exploited spectral RSDs retrieved with high time and vertical resolution thanks to a new technique combining multifrequency radar observations (Tridon & Battaglia, 2015). In these studies, comparisons between rain microphysics properties derived from these state-of-the-art observations and simulated with the Weather Research and Forecasting (WRF) Model (Skamarock et al., 2008) highlighted significant discrepancies. In particular, the profile of the mean volume diameter and concentration parameter are not well reproduced by the model and these inaccuracies can have a marked impact on the simulated evaporation rate.

The work presented here is a continuation of the studies made by Tridon et al. (2019b) and Planche et al. (2019). From the analysis of observed RSD variations in the atmosphere, the aim is to evaluate the most popular parameterizations of raindrop self-collection and breakup processes used in two-moment bulk schemes of numerical weather prediction (NWP) models : the parameterizations of Ziegler (1985), Seifert (2008) and Morrison et al. (2012), corresponding respectively to the microphysics schemes used in Meso-NH (Lafore et al., 1998; Lac et al., 2018), ICON (ICOsahedral Non-hydrostatic; Wan et al., 2013) and WRF (Skamarock et al., 2008). In this framework, the objective is to provide a new parameterization of these microphysical processes.

In this paper, the different representations of the raindrop self-collection and breakup processes in bulk models are described in Section 2. Section 3 presents observation data and case studies. Section 4 explains the analysis method developed in this study and the results are shown in Section 5. Section 6 summarizes the study and the main findings.

2 Representation of the raindrop self-collection and breakup processes in bulk models

2.1 Self-Collection process parameterization

There are several rain microphysical processes that affect the vertical evolution of the RSD. One of the most important and most often studied is the raindrop self-collection process. In general, a parameterization of the self-collection process in bulk numerical models (e.g. Ziegler, 1985; Beheng, 1994; Seifert & Beheng, 2001) is based on the resolution of the stochastic collection equation (SCE) which describes analytically the rate of change of a drop spectrum under the effects of collision between drops and their eventual subsequent collection or breakup (Pruppacher & Klett, 1997).

Many methods have been proposed for solving the SCE (Bleck, 1970; Gelbard & Seinfeld, 1978; Tzivion et al., 1987; Brown, 1993; Hu & Srivastava, 1995; Seesselberg et al., 1996; Bott, 1998). Each of these methods proposed some improvements with regards to those already existing, e.g. by considering evaporation or collisional breakup. However, most of these methods suffered from important numerical diffusion leading to an artificial broadening of the drop spectrum (for more details, see the overview made by Prat & Barros, 2007). Berry & Reinhardt (1974) managed to overcome the numerical diffusivity by using an interpolation at intermediate points of the

discretization. Furthermore, they proposed the concept of "large hydrometeor self-collection" and showed that it is essential for the rapid growth of large hydrometeors. It is one of the most popular methods and is at the basis of the parameterizations of self-collection used in bulk schemes.

By numerically solving the SCE, Long (1974) proposed a polynomial approach leading to results close to the spectral solution. As in Berry and Reinhardt (1974), he found two different polynomial expressions for cloud droplets and raindrops growth regimes. Ziegler (1985) proposed a parameterization of the raindrop self-collection process in a bulk scheme based on Long (1974) results. It represents the evolution of the total concentration of raindrops as a function of time:

$$\frac{dN_\mathrm{r}}{dt} = \begin{cases} -\alpha\ RWC^2, & D < 0.1\ mm \\ -\beta\ N_\mathrm{r}\ RWC, & D \geq 0.1\ mm \end{cases} \quad \text{(Equation 1)}$$

where N_r is the total concentration of raindrops (in m^{-3}), RWC is the rain water content (in kg m^{-3}), D is the diameter, $\alpha = 5.66 \times 10^{10}$ m^3 kg^{-2} s^{-1} and β = 5.78 m^3 kg^{-1} s^{-1} are weighting factors. In his approach, Ziegler (1985) assumes that the RSD *N(v)* can be represented by a gamma distribution, with a shape parameter υ_r, as function of the volume of raindrops *v*. Note that α was obtained by simplifying Eq.A16 of Ziegler (1985), taking a value υ_r equal to -0.8, as mentioned in his section 2.

Following Wood (2006), we rewrite Equation 1 as function of the raindrop size rather than the RWC. Equation 1 becomes:

$$\frac{dN_\mathrm{r}}{dt} = \begin{cases} -\alpha_\mathrm{W}\ N_\mathrm{r}^2\ D_\mathrm{mv}^6, & D < 0.1\ mm \\ -\beta_\mathrm{W}\ N_\mathrm{r}^2\ D_\mathrm{mv}^3, & D \geq 0.1\ mm \end{cases} \quad \text{(Equation 2)}$$

with $\alpha_W = 1.55 \times 10^{16}$ m^{-3} s^{-1} and $\beta_W = 3{,}026$ s^{-1}, and where D_mv is the mean volume diameter (in m) defined as follows:

$$D_{mv} = \left(\frac{M_3}{M_0}\right)^{1/3} \quad \text{(Equation 3)}$$

where M_0 and M_3 are respectively the zeroth and the third moments of the raindrop size distribution *N(D)* and the moment of degree i is defined as $M_\mathrm{i} = \int_0^\infty D^i\ N(D)dD$. In general, *N(D)* is represented in bulk models by a gamma distribution $N(D) = N_0 D^\mu e^{-\lambda D}$, where N_0, μ and λ are, respectively, the concentration, shape and slope parameters.

In most bulk models, Equation 1 is used to calculate the temporal evolution of the raindrop concentration. For example, the self-collection parameterization of Ziegler (1985) is also used in the scheme of Morrison et al. (2009, 2012). The parameterization of Seifert and Beheng (2001) is the same as Ziegler (1985) (Equation 1) but with a threshold diameter (D_{th}) of 0.08 mm and a different value of the weighting factor α_S (equal to 4.33 m^3 kg^{-1} s^{-1} in the Equation 1 and equal to 2,270 s^{-1} in the Equation 2) as found by Seifert (2002). Another self-collection parameterization was developed by Seifert (2002) and Seifert and Beheng (2006) but was not further considered in Seifert (2008) where the parameterization defined in Seifert and Beheng (2001) was preferred because it was in better agreement with reference simulations (Seifert, 2023, personal communication).

2.2 Breakup process parameterization

Another process which influences the RSD is the collisional breakup of large raindrops. It limits the maximum size that raindrops can reach and redistribute the size spectrum via the formation of multiple smaller drops (breakup fragments). Studies on the collisional drop breakup showed that three types of drop breakup exist (filaments, sheets and disks) (McTaggart-Cowan & List, 1975; Low & List, 1982a) and concluded that filament breakup is the most active mode for drops smaller than 3 mm (Low & List, 1982a). Besides, using model simulations, Srivastava (1978) suggested that spontaneous breakup is negligible compared to collisional breakup. More recently, Paukert et al. (2019) stated that the process rate of spontaneous breakup becomes comparable to that of collisional breakup around D_r = 1.1 mm equivalent to D_{mv} = 2 mm (note that this size is the limit of the studies mentioned below and outside of the observed size range used in our study).

In order to consider the breakup process, Ziegler (1984, 1985) introduced the so-called rain self-collection efficiency parameter (E_c) in the self-collection parameterization (by multiplying the right-hand side of Equation 1 by E_c) which results in a reduction of the overall collection rate for large drops. Based on the coalescence efficiency of Brazier-Smith et al. (1972) for drop size smaller than 1 mm and on the experiments of Low and List (1982a) on drops ranging from 0.4 to 4 mm, Ziegler (1985) defined the following parameterization for E_c:

$$E_c = \begin{cases} 1, & D_{mv} < 0.6\ mm \\ \exp[-2.5(D_{mv} - 0.6)], & 0.6 \leq D_{mv} < 2\ mm \\ 0, & D_{mv} \geq 2\ mm \end{cases} \quad \text{(Equation 4)}$$

which has been rewritten as function of D_{mv} (Equation 3) which is simply twice the mean volume radius used by Ziegler (1985).

Thereby, when the rain self-collection efficiency (E_c) is equal to 1, the breakup process has no effect (self-collection is the only active process). When $0 < E_c < 1$, breakup starts to be active but the self-collection process still dominates the evolution of the RSD, while if E_c is negative, it is the breakup process which dominates. Finally, if E_c is equal to 0, the self-collection and breakup processes compensate each other and in this case, the raindrop size distribution (RSD) is at equilibrium (Hu & Srivastava, 1995; Seifert, 2008; Barthes & Mallet, 2013). For example, with the parameterization of Ziegler (1985) (Equation 4), E_c is never negative, so the breakup process never dominates.

Other expressions of E_c have been proposed to describe the raindrop breakup in bulk microphysics schemes. In Morrison et al. (2009, 2012), the E_c parameter is defined according to Equation 5 which corresponds to a modified version of the E_c expression developed by Verlinde and Cotton (1993):

$$E_c = \begin{cases} 1, & D_{mv} < D_{mv,th} \\ 2 - \exp\left[A\left(D_{mv} - D_{mv,th}\right)\right], & D_{mv} \geq D_{mv,th} \end{cases} \quad \text{(Equation 5)}$$

Note that in Morrison et al. (2012), the expression was written as function of the mean diameter $D_r = M_1/M_0$. Hence, Equation 5 has been rewritten as function of D_{mv} which relates to D_r according to $D_{mv} = D_r \frac{[(\mu+3)(\mu+2)(\mu+1)]^{(1/3)}}{\mu+1}$. When μ equals 0 (assumption made in the Morrison scheme), A = 1,266 m^{-1}. In Equation 5, $D_{mv,th}$ is the threshold mean volume diameter from which the breakup

starts to be effective. In Morrison et al. (2012), $D_{mv,th}$ is equal to 0.54 mm (hereafter called Morr-CTL) (note that this is different from the expression developed in Verlinde and Cotton (1993) where $D_{mv,th}$ = 1.09 mm). To evaluate the impact of the breakup process on rain properties, Morrison et al. (2012) modified the threshold mean volume diameter ($D_{mv,th}$) of Equation 5 considering $D_{mv,th}$ = 0.19 mm or $D_{mv,th}$ = 0.93 mm in order to obtain a breakup process more or less efficient, respectively (note that this corresponds to threshold mean diameter ($D_{r,th}$) of 105 and 510 μm and these parameterizations are thereafter called Morr-105 and Morr-510, respectively).

A breakup parameterization has also been developed by Seifert and Beheng (2006) as part of the development of their two-moment microphysics scheme. To this end, a spectral model was used to solve the stochastic collection/breakup equation using the breakup parameterizations of Low and List (1982a) and Beard and Ochs (1995). Contrary to Morrison et al. (2009, 2012), Seifert (2008) assumes gamma distributions ($\mu \neq 0$) and a relation between the shape (μ) and the slope (λ) parameters of the RSD. Following Verlinde and Cotton (1993), the resulting parameterization contained an additional expression for large drops (mean diameter greater than 0.9 mm) in order to eliminate the size sorting artifact, which is a well-known issue for two-moment schemes (Wacker & Seifert, 2001; Mansell, 2010; Milbrandt & McTaggart-Cowan, 2010; Ziemer & Wacker, 2012). However, this condition has been later excluded because the μ-λ relation used by Seifert (2008) avoids the size sorting effect and the additional condition of Verlinde and Cotton (1993) is no longer necessary (Seifert, 2023, personal communication).

$$E_c = \begin{cases} 1, & D_{mv} \leq 0.3\ mm \\ -\gamma\ (D_{mv} - D_{mv,eq}), & D_{mv} > 0.3\ mm \end{cases} \quad \text{(Equation 6)}$$

where γ = 1 mm^{-1} (equivalent to k_{br} in Seifert, 2008) and the equilibrium mean volume diameter $D_{mv,eq}$ = 1.1 mm.

Figure 1 presents the different parameterizations of the rain self-collection efficiency (E_c) provided in this section as a function of the mean volume diameter (D_{mv}). This figure shows that the approach of Ziegler (1985) (Z85) considers that the self-collection process is always the dominant process since E_c remains larger than zero. Interestingly, the representations of Morr-CTL and Seifert (2008) (S08) are very different, but for both of them, the self-collection process is dominant when D_{mv} is lower than 1.1 mm whereas the breakup process becomes dominant for larger sizes. In other words, Morr-CTL and S08 assume the same equilibrium diameter (D_{mv} = 1.1 mm). Moreover, as mentioned before, additional expressions were proposed in Morrison et al. (2012) to conduct some sensitivity tests by modifying the $D_{mv,th}$ parameter in Equation 5. This results in a more (Morr-105) or less (Morr-510) efficient breakup process compared to Morr-CTL: the breakup process becomes dominant when D_{mv} > 0.75 mm in Morr-105 and when D_{mv} > 1.45 mm in Morr-510 (Figure 1).

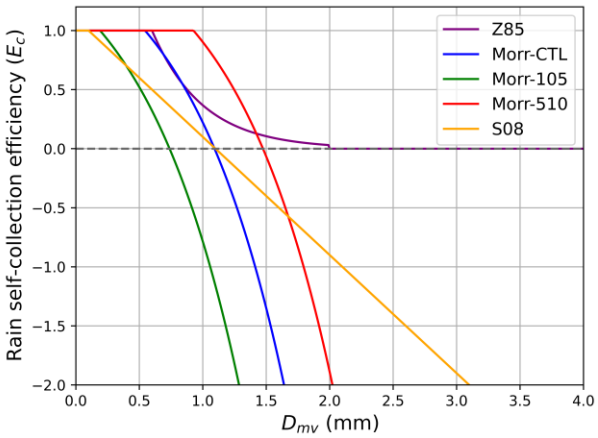

Figure 1. Rain self-collection efficiency E_c as a function of mean volume diameter D_{mv} as parameterized in Ziegler (1985) (Z85; in purple), in Seifert (2008) (S08; in orange) and in Morrison et al. (2012) with a threshold mean diameter for breakup $D_{r,th}$ of 0.300 mm (Morr-CTL; in blue), 0.105 mm (Morr-105; in green) and 0.510 mm (Morr-510; in red). Note that to avoid an unrealistic discontinuity in the representation of the S08 expression, we have taken a threshold mean volume diameter value $D_{mv,th}$ of 0.1 mm instead of 0.3 mm (see Equation 6).

In summary, Figure 1 illustrates how these parameterizations lead to a vastly different dependence of E_c on D_{mv} and hence, clearly shows the extreme variability in the representation of the self-collection and breakup processes in two-moments bulk models. For example, considering a mean volume diameter D_{mv} = 1.3 mm, the raindrop size distribution would evolve as if the self-collection process were dominant in Morr-510 and Z85 whereas it would evolve as if the breakup process were dominant in Morr-CTL, Morr-105 and S08. Thus, more RSD observations in natural clouds and precipitation such as those derived from multifrequency radar observations could be very helpful to evaluate the relevance of these representations.

3 Description of observation data and case studies

Since 2000s, the combination of observations from multiple radars operating at different frequencies has led to the development of novel retrieval techniques providing the microphysics properties of clouds and precipitation with more accuracy, for both the ice phase (Leinonen et al., 2018; Mason et al., 2018; Tridon et al., 2019a, 2022; Mroz et al., 2021; Billault-Roux et al., 2023, among others) and the liquid phase (Mason et al., 2017; Tridon et al., 2017a, 2019b; Mroz et al., 2020, among others). So far, such innovative microphysics retrievals have been applied at very few locations in the world due to both complex instrumental settings and complex inversion methods.

For rainfall, Tridon and Battaglia (2015) and Tridon et al. (2013a, 2017a) have developed a retrieval technique which combines the Doppler spectra profiles observed by two collocated vertically pointing K_a- and W-band radars and retrieves the profiles of the binned RSD together with vertical wind and Doppler spectra broadening due to turbulence. This retrieval has been applied to one case study observed at Hyytiälä in Finland during the Biogenic Aerosols Effects on Clouds and Climate (BAECC) field campaign (Tridon et al., 2017a) and one case study observed at the Southern Great Plain (SGP) Atmospheric Radiation Measurement (ARM) Central Facility in Oklahoma (USA) (Tridon et al., 2019b). The two cases correspond respectively to a midlatitude stratiform precipitation event observed on 7 June 2014 at Hyytiälä (Finland) and a squall-line

system observed on 12 June 2011 at the SGP site (OK, USA). Due to the complexity of the instrumental setup and of the retrieval methodology, these are the only two case studies available for our analysis. Nevertheless, they showcase two contrasting precipitation cases corresponding to two different types of precipitation systems (squall line vs. frontal system), observed in two different regions of the globe (close to the sub-tropics vs. the Arctic) and including different ranges of drop diameters, hence allowing to assess the generality of our results.

For both case studies, a similar instrumental set is used since the U.S. Department Of Energy (DOE) ARM program deployed the second ARM Mobile Facility in Hyytiälä during the BAECC campaign (Petäjä et al., 2016; Kollias et al., 2020), i.e. the K_a-band ARM zenith radar (KAZR) (ARM user facility, 2014a; ARM user facility, 2011a) collocated with a W-band radar (the Marine W-band ARM Cloud Radar (MWACR) for the Finland case, ARM user facility, 2014b and the W-band Scanning ARM Cloud Radar (WSACR) for the Oklahoma case, ARM user facility, 2011b). The main difference between the two later radars is the scanning capability of the WSACR but it was exceptionally operated in zenith pointing for the whole duration of the squall line event, hence vertical profiles of Doppler spectra have been provided with high temporal resolution for the whole duration of both cases studies.

Figure 2 represents the time-height evolution of the radar reflectivity fields obtained with the KAZR (Figure 2a) and the MWACR (Figure 2b) for the Finland case. Differences in reflectivity (Figures 2a-b) are due to the dependence of hydrometeor scattering and extinction cross section on the radar frequency for mm-wavelength radars (e.g. as described by Mie theory when assuming spherical raindrops). Generally, the backscattering cross section of large hydrometeors decreases with radar frequency while the overall extinction increases, eventually leading to the complete extinction of the radar signal (e.g. at 3 km height around 12:25 UTC for the MWACR). Figure 2 shows that the event over Finland lasts approximately 4.5 hours, with a cloud top height varying between 5 and 8 km. The 0°C isotherm altitude is around 2.5 km as highlighted by the clear difference between low-reflecting ice crystals and highly-reflecting raindrops. Different periods of precipitation can be identified, with initial light shallow showers followed by some deeper precipitation evolving into a homogeneous period of stratiform rain, between 12:20 and 13:40 UTC.

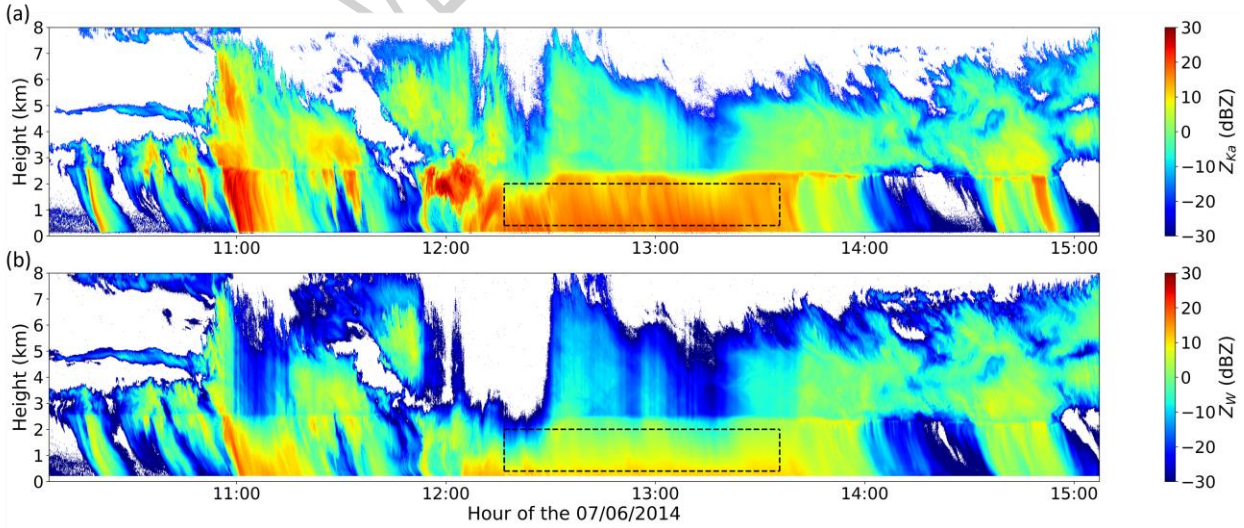

Figure 2. Time-height evolution of the ARM K_a-band radar reflectivity (KAZR) (a) and the W-band radar reflectivity (MWACR) (b) for the Finland case. The area framed in black represents the period studied. The x axis label corresponds to the hour of the dd/mm/yyyy.

Similarly, Figure 3 shows the radar reflectivity fields obtained with the KAZR (Figure 3b) and the WSACR (Figure 3c) for the Oklahoma case. At the SGP site, the ultrahigh-frequency (UHF) radar wind profiler (RWP; ARM user facility, 1998) reconfigured in precipitation mode was also available. At this frequency (915 MHz, corresponding to a wavelength of 33 cm), the interaction with hydrometeors can be described by the Rayleigh approximation and their extinction is negligible (Tridon et al., 2013b). Figure 3a shows the corresponding time-height evolution of the radar reflectivity field and presents the three typical regions of a squall-line system: the convective region (CR) with a cloud top reaching 12 km and heavy precipitation (leading to complete extinction of WSACR signal as low as 1 km), the transition zone (TZ) with moderate precipitation and the stratiform region (SR) characterized by its bright band highlighting the ice crystals melting zone (i.e. the 0°C isotherm altitude which is located at around 3.5 km).

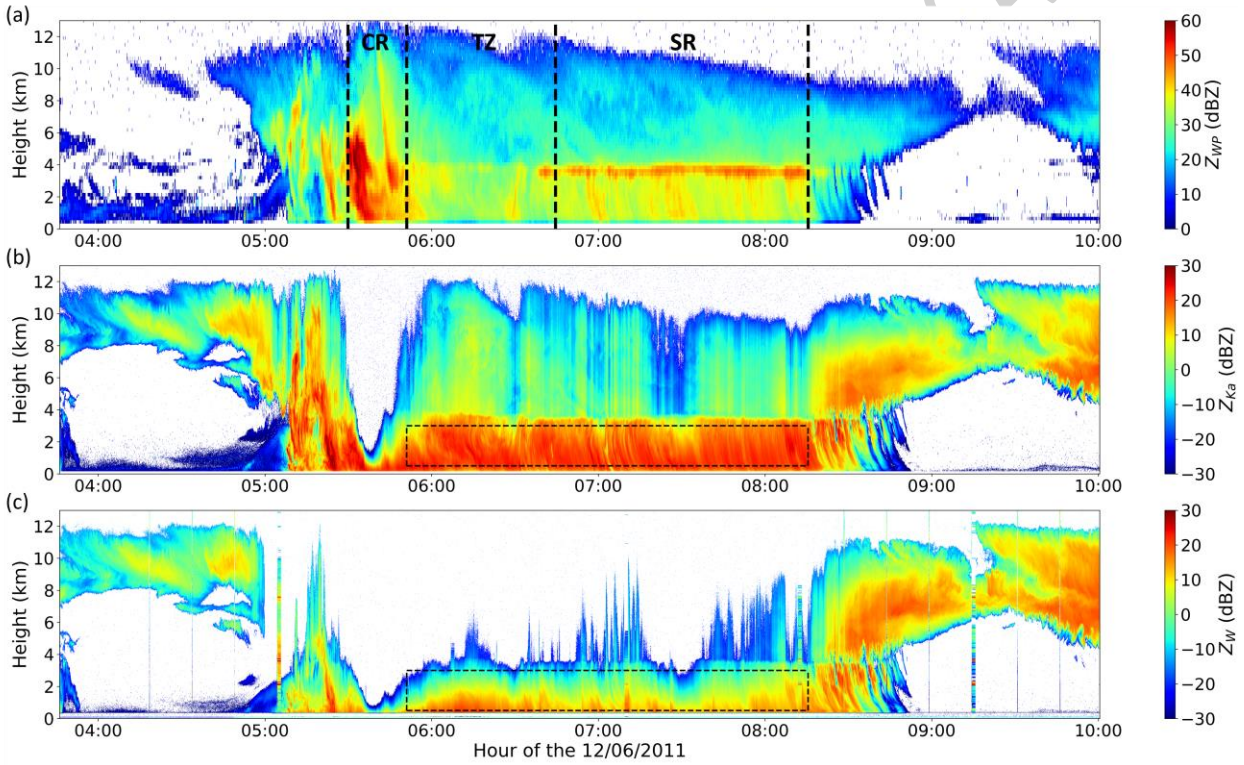

Figure 3. Time-height evolution of the ARM UHF radar wind profiler (RWP) reflectivity (a), the K_a-band radar reflectivity (KAZR) (b) and the W-band radar reflectivity (WSACR) (c) for the Oklahoma case. The vertical dashed lines (a) represent the three periods (CR: Convective Region, TZ: Transition Zone and SR: Stratiform Region) of the squall line defined in Section 3. The area framed in black represents the period studied. Note that the color scale is different in Figure 3a. The x axis label corresponds to the hour of the dd/mm/yyyy.

For our study, we rejected the observations of the convective rain periods because of the heavy rain leading to strong attenuation and of the intense updrafts which makes the analysis method described in Section 4 inapplicable. Moreover, the melting process is not instantaneous and crystals can melt over few hundred meters in stratiform situations (see e.g. Planche et al., 2014). Thus, to avoid the presence of melting crystals, we restricted the analysis to data 500 m below the 0°C isotherm altitude. The periods studied are shown in Figures 2 and 3 (areas framed in black) for respectively the Finland case and the Oklahoma case. Note that the Doppler spectra

were recorded with higher temporal resolution during the Finland case. Thus, for the Finland case, this period lasts from 12:15 to 13:35 UTC (equivalent to 2,309 observed vertical profiles) while for the Oklahoma case, it lasts from 5:50 to 8:15 UTC encompassing the transition zone (TZ) and the stratiform region (SR) (equivalent to 2,355 observed vertical profiles).

The multifrequency radar retrieval was applied on the Finland and Oklahoma cases by Tridon et al. (2017a) and Tridon et al. (2019b), respectively, and provides estimates of the profiles of the binned RSD and the vertical wind w, and their uncertainties, with high resolution in the vertical (30 m) and in time (2 s for the Finland case and 4 s for the Oklahoma case). From the binned RSD, other parameters can be derived. For example, Tridon et al. (2017a) and Tridon et al. (2019b) described the time-height variations of the mean volume diameter $D_{\mathrm{m}} = M_4/M_3$, the concentration parameter N_0^* (Testud et al., 2001) and the rain mixing ratio q_{r}, in their Fig. 6 and Fig. 8 for the Finland case and the Oklahoma case, respectively. Time-height evolutions of the mean volume diameter D_{mv}, the total raindrop concentration N_{r} and the rain water content RWC, i.e. the parameters used in the present work for the parameterization of the self-collection and breakup processes (Equations 1 and 2) are given in Figures S1 and S2 of the Supplementary material for both cases.

Figure 4 presents the profile of the RSD averaged over 150 m and 1-min, at 13:00 UTC for the Finland case and 7:45 UTC for the Oklahoma case. It shows that the concentration of the smallest raindrops (D < 1.5 mm) decreases substantially with altitude in both cases. For the largest drops (D > 2.5 mm), the raindrop concentration increases towards the surface for the Finland case (Figure 4a) whereas it slightly decreases for the Oklahoma case (Figure 4b). Note that for the Oklahoma case, the vertical trend remains similar for all sizes independently of the period selected (e.g. when considering the TZ or SR regions solely) while it is fairly variable for the Finland case (not shown). Figures 4c and 4d represent the temporal evolution of the 1-min averaged RSD at 1 km height for the Finland and Oklahoma case, respectively. For the Finland case (Figure 4c), there are more large raindrops (D_{max} > 6 mm) at the beginning of the analyzed period (also visible in Figure S1). For the Oklahoma case, RSDs from the transition zone (from 5:50 to 6:50 UTC) are different to those from the stratiform zone (from 6:50 to 8:15 UTC). The maximum diameter of the TZ is smaller (around 3-4 mm) than that of the SR (around 5-6 mm). In both cases, the variability of the RSDs is larger in time than in the vertical, suggesting that the variability of rainfall over time is greater than the variability due to the self-collection and breakup processes themselves (since they affect primarily the vertical variability of the RSD). This emphasizes the complexity of highlighting the fingerprints of these processes from observations since they must be first disentangled from the rainfall natural variability.

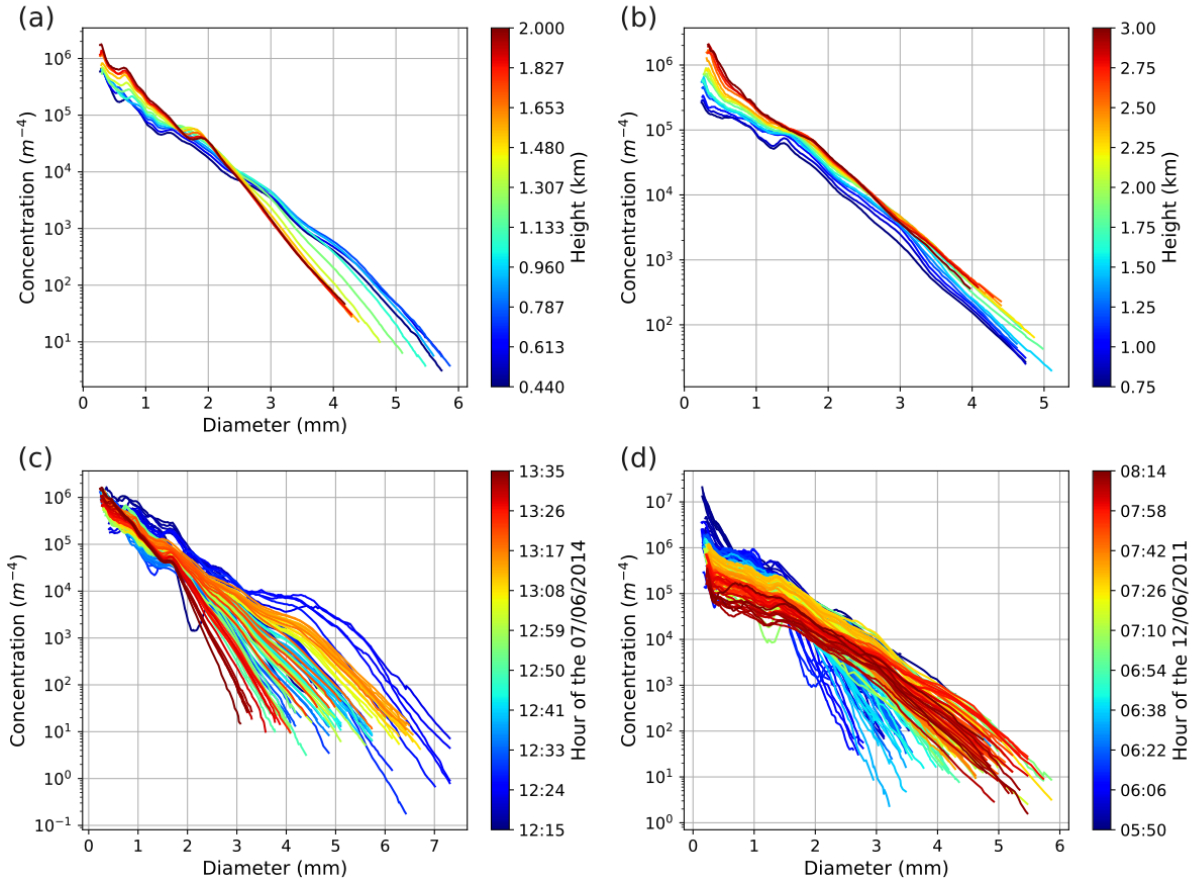

Figure 4. Vertical evolution of the averaged binned RSD profiles obtained every 150 m of altitude (in a.g.l) and 1 min, at 13:00 UTC for the Finland case (a) and at 7:45 UTC for the Oklahoma case (i.e., TZ and SR) (b). These periods correspond to the areas framed in black in Figures 2-3. Time evolution of the averaged binned RSD obtained every 1 min at 1 km for the Finland case (c) and for the Oklahoma case (d).

From the time-height evolution of the retrieved parameters (D_{mv}, N_r and RWC, shown in Figures S1 and S2), we can derive the profiles of their probability density functions (also called Contoured Frequency by Altitude Diagrams, CFAD) for both case studies (Figure 5). For the Finland case (Figure 5a, c, e), we observe an increase of the mean volume diameter D_{mv} towards the ground from 0.8 to 1.1 mm combined with a decrease of the total raindrop concentration N_r from around 600 to 300 m^{-3}. The corresponding RWC values range from 0.1 to 0.3 g m^{-3} and show a slight decrease towards the ground. The observed multi-modality is probably due to the fact that the Finland case shows several clearly distinct rainfall regimes (see Figure S1c). For the Oklahoma case (Figure 5b, d, f), the trends are similar to those of the Finland case, but with a greater dispersion of the data (in particular for N_r) because we combine two clearly distinct periods (TZ and SR). In TZ, mean volume diameters and total raindrop concentration range from 0.8 to 1.1 mm and from 200 to 5,000 m^{-3}, respectively, while in SR, they range from 1 to 1.4 mm, and 80 to 2,000 m^{-3} (see Figures S2a and S2b). The variation in RWC is more marked in the Oklahoma case, with a decrease of the mean values towards the surface from 0.4 to 0.2 g m^{-3}.

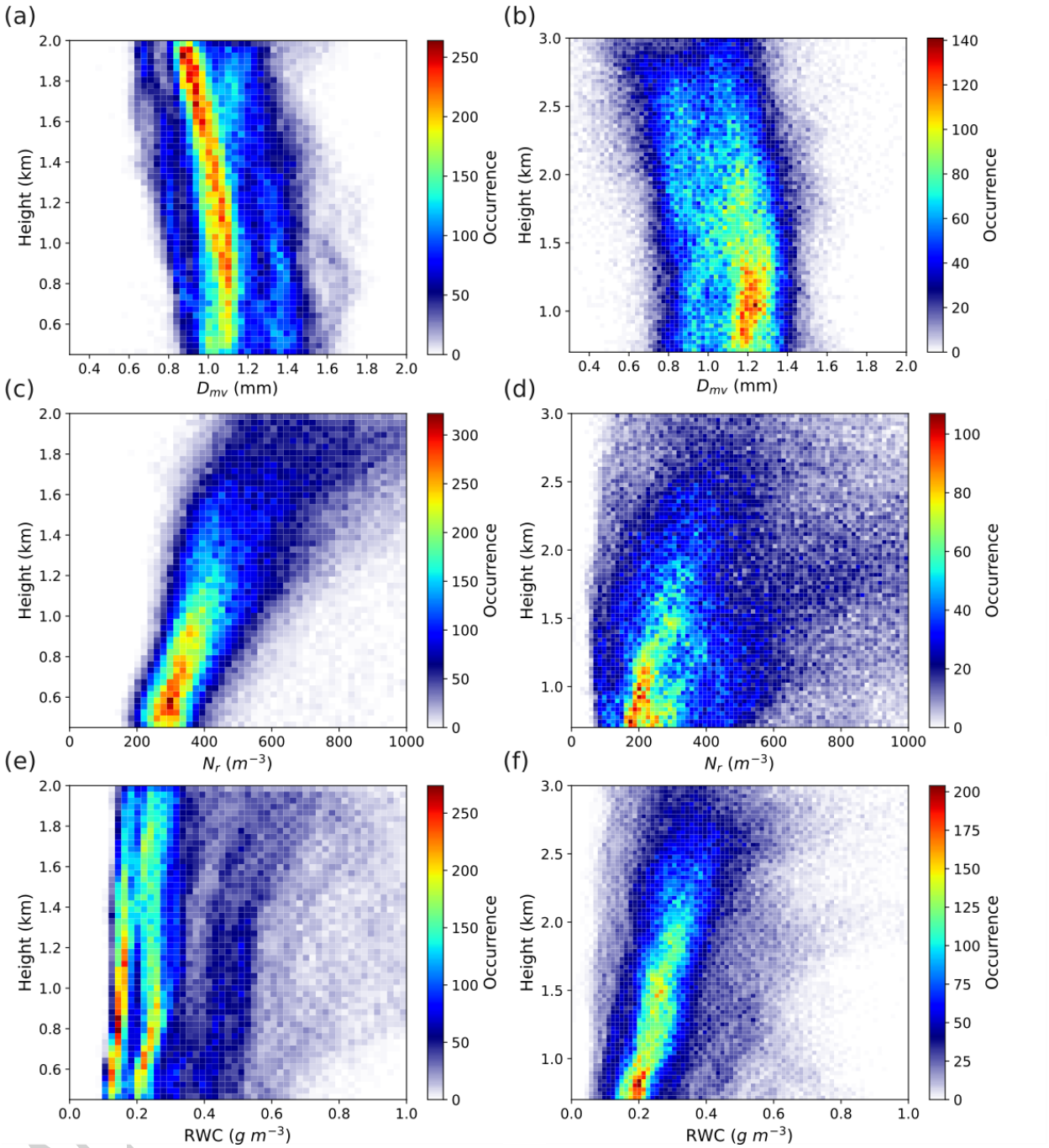

Figure 5. Profile of the probability density functions of (a, b) the mean volume diameter (D_{mv}), (c, d) the total raindrop concentration (N_r) and (e, f) the rain water content (RWC) for Finland case (a, c, e) and for Oklahoma case (b, d, f). Note that the y-axis is different according to the case study and that the color scales are different.

4 Analysis method

In addition to the processes of self-collection and breakup, the spatiotemporal evolution of the RSD can also be affected by dynamics (advection) and thermodynamics processes (condensation/evaporation). All these processes are dependent on the raindrop sizes (D). For example, while, in a first approximation, the horizontal wind transports all raindrops equally, their

distinct fall velocities impinge the time they remain in an atmospheric layer and hence their overall advection. While a one-dimensional sedimentation approach is often used (see e.g. Prat et al., 2008), we applied hereafter the two-dimensional framework proposed by Marshall (1952) taking into account the combined effect of fall velocity (V_t), vertical wind (w) and horizontal wind speed (u) on the spatiotemporal evolution of raindrops in order to reconstruct the trajectories of different raindrop sizes as retrieved by the vertically pointing radar. Thus, for this purpose, we used the technique of Hogan and Kew (2005) for determining the trajectories of the raindrops according to their diameters D. The numerical approach of Hogan and Kew (2005) calculates iteratively the horizontal displacement $x_D(z)$ at an altitude z from a reference level z_{ref}:

$$x_{\mathrm{D}}(z_{k-1}) = x_{\mathrm{D}}(z_k) + \left(u(z_{k-1}) + u(z_k) - 2u_{ref}\right)\frac{(z_{k-1}-z_k)}{\left[\left(V_{\mathrm{t,D}}(z_{k-1})-w(z_{k-1})\right)+\left(V_{\mathrm{t,D}}(z_k)-w(z_k)\right)\right]}$$

(Equation 7)

The reference level z_{ref} (e.g. the top of the observed rain field) moves horizontally with the wind speed u_{ref}, thus $x_D\left(z_{k=ref}\right) = 0$. The horizontal wind speed u at each level k is derived from the radiosonde data collected at the measurement sites and on the specific dates of both the Oklahoma (at SGP on 12 June 2011) and the Finland (at Hyytiälä on 7 June 2014) cases while the vertical wind speed w at each altitude z is provided by the multifrequency radar retrieval. Following Tridon and Battaglia (2015), the terminal fall velocity of raindrops $V_t(D)$ (in m s^{-1}) is parameterized using both expressions of Frisch et al. (1995) and Atlas et al. (1973) for small and large diameters, respectively:

$$V_{t,D}(z_k) = \begin{cases} \left[41.6 \times 10^2\, D - 0.083\right]\left(\frac{\rho_0}{\rho(z_k)}\right)^{0.5}, & D < 0.86\, mm \\ \left[9.65 - 10.3\exp(-6 \times 10^2\, D)\right]\left(\frac{\rho_0}{\rho(z_k)}\right)^{0.5}, & D \geq 0.86\, mm \end{cases} \quad \text{(Equation 8)}$$

where ρ_0 and $\rho(z_k)$ are, respectively, the air densities at 1000 hPa and at the measurement altitude z_k, and D the diameter (in m). Equation 7 describes the trajectories of the raindrops in terms of their displacement with respect to their initial positions at z_{ref}. However, to exploit the radar retrieval, the raindrop trajectory is needed in the time-height space of the radar observations. This is possible if the properties of the raindrops observed at the time $t + dt$ over the radar are sufficiently correlated with the properties of the raindrops observed at the time t at a distance udt upstream from the radar. In other words, these raindrops need to be assumed to belong to the same fallstreak of precipitation. In this way, Equation 7 takes into account the differential trajectory of raindrops due to their different fall velocities and the variation of the raindrop concentration in each size bins within the time dt can be attributed to the microphysics processes only. Supposing that the rain field moves during the time interval dt over the radar by a distance $u_{ref}dt$, we can allocate the trajectory of the raindrops at altitude z_k to the time of the radar observation as:

$$t_{\mathrm{D}}(z_k) = x_{\mathrm{D}}(z_k)/u_{ref} \quad \text{(Equation 9)}$$

Figure 6 presents an example of the time-height evolution of the concentrations (N) of 1-mm (Figure 6a) and 2-mm (Figure 6b) diameter raindrops per unit size (in m^{-4}) for the Finland case. The black solid lines indicate the predicted trajectories for these two sizes of raindrops. Starting from the same position ($z_{ref} = 2\ km$), we can see that the spatiotemporal evolutions of the 1-mm and 2-mm diameter raindrops are different. The trajectories of the 1-mm diameter raindrops (Figure 6a) are more curved than those of the 2-mm diameter raindrops (Figure 6b). Indeed, the larger the raindrops the faster they fall and the less they are affected by the horizontal wind. Note

also the differences between the radar retrieved fallstreaks for 1 mm (Figure 6a) and 2 mm raindrops (Figure 6b).

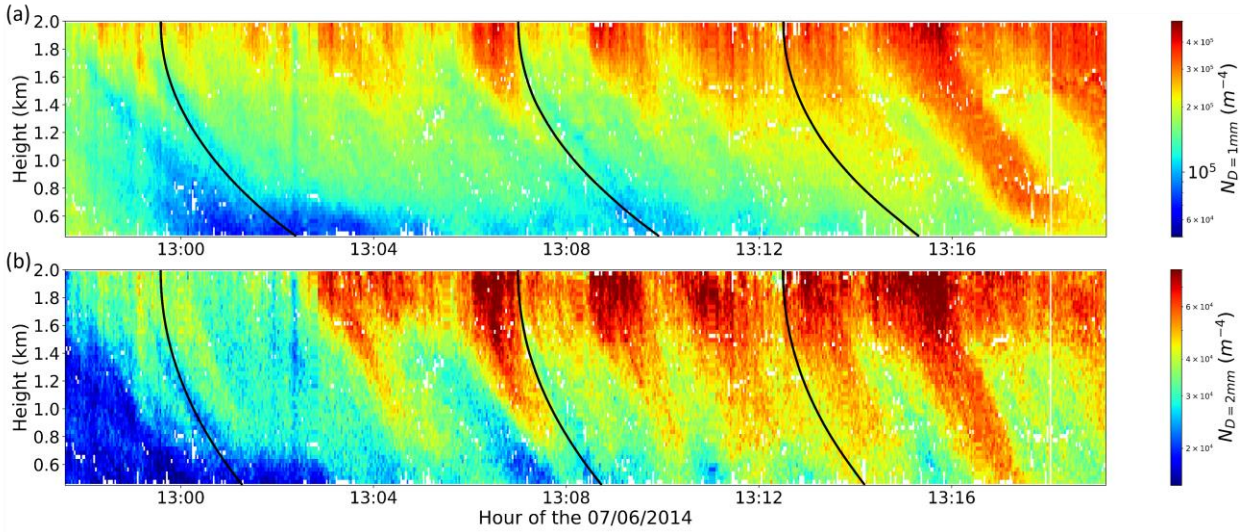

Figure 6. Time-height evolution of the 1-mm (a) and 2-mm (b) raindrop concentrations *N* per unit size (in m^{-4}) for the Finland case. The black solid lines represent the trajectories obtained for these specific sizes. The x axis label corresponds to the hour of the dd/mm/yyyy.

Following the trajectories of each raindrop diameter (*D*) included in the observed size range (i.e., from 0.4 to 6 mm), we can determine the vertical variation of the concentration of these raindrops between successive levels by:

$$\frac{dN_D}{dz}(z_k) = \frac{N_D(t_D(z_{k+1})) - N_D(t_D(z_{k-1}))}{z_{k+1} - z_{k-1}} \quad \text{(Equation 10)}$$

This methodology is illustrated in Figure 7 which represents the trajectory of a 1-mm and a 2-mm raindrop (blue and red curve, respectively) with the same starting time and position. The grid represents the time and height resolution of radar observations for the Finland case (4 s and 30 m). The position of the 1 mm (2 mm) raindrop during its fall is represented by the blue (red) crosses at each altitude z_k, and the closest radar pixel is highlighted by the colored blue (red) boxes. Then, the concentrations corresponding the selected radar pixels are used in Equation 10.

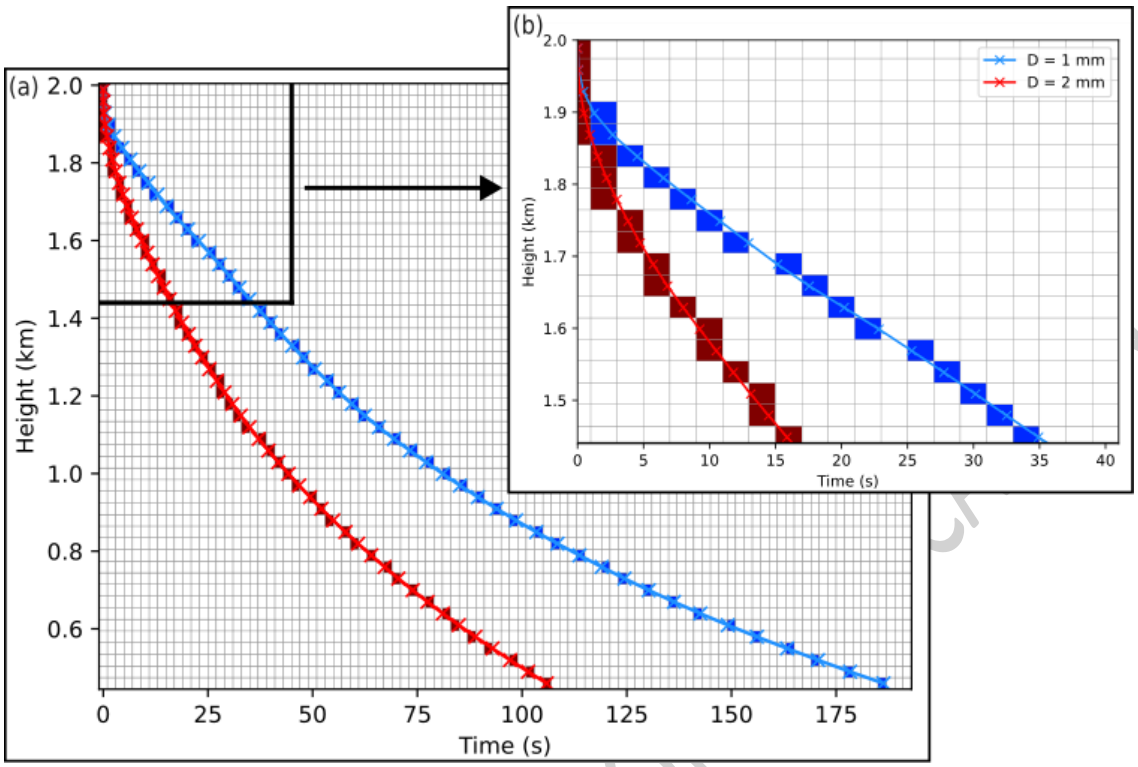

Figure 7. (a) Example of trajectory of a 1-mm (in blue) and a 2-mm (in red) raindrop at 12:15 UTC for the Finland case as a function of height (in km) and time (in s). (b) A zoom to show these trajectories between 2 and 1.44 km. The crosses and the colored boxes (blue for D = 1 mm and red for D = 2 mm) represent the position of the raindrop at each altitude z_k, and the closest radar pixel, respectively.

The temporal variation as sampled by the radar of the concentration of these raindrops $\frac{dN_D}{dt}(z_k)$ for each altitude z_k is then given by:

$$\frac{dN_D}{dt}(z_k) = \frac{dN_D}{dz}(z_k)\left(V_{t,D}(z_k) - w(z_k)\right) \qquad \text{(Equation 11)}$$

where *dt* now represents the "physical time step" and not the time separation between radar observations. Then, the temporal variation of the total concentration of raindrops $\left(\frac{dN_r}{dt}\right)$ is calculated by integrating $\frac{dN_D}{dt}$ over all diameters *D*:

$$\frac{dN_r}{dt}(z_k) = \int_{D_{min}}^{D_{max}} \frac{dN_D}{dt}(z_k)\, dD \qquad \text{(Equation 12)}$$

where D_{min} and D_{max} correspond to the minimum and maximum diameters retrieved by the radar retrieval. Equation 12 permits to study the variations of the raindrop concentration due to microphysical processes from the radar observations. The objective of Section 5 is to determine if such an analysis could highlight some fingerprints of the raindrop self-collection and breakup processes.

In this method, we argue that the effect of evaporation of raindrops has a negligible impact on the raindrops trajectory within two successive vertical layers of the radar retrieval (resolution of 30 m). Even if the variation of the total concentration due to evaporation and to self-collection and breakup can be of the same order of magnitude, the fingerprint of self-collection and breakup rates can possibly be retrieved because the evaporation leads to a local change of concentration (the overall effect of evaporation is a shift of the drop concentration in each diameter towards a slightly lower diameter as shown in Tridon et al., 2017b), while self-collection and breakup

processes shift the raindrops over significantly different diameters. We verified the validity of this assertion by calculating the effect of evaporation on the trajectory of raindrops thanks to the equations described in Kumjian and Ryzhkov (2010): we compared the trajectory of a raindrop in the radar time-height observation space with and without taking into account the evaporation process for various drop sizes and relative humidities (RH). After 60 m of fall, this results in a maximum time difference of 0.1 s for a drop of 0.4 mm and a RH of 5%, and the time difference decreases quickly with increasing diameter. This confirms that for the range of diameters (D > 0.4 mm) and RH (~50%) considered in our study, the effect of evaporation on the raindrops trajectory is negligible in comparison to the radar sampling resolution of around 2 s.

5 Results

To evaluate the parameterizations of self-collection and breakup presented in Section 2 with the multifrequency radar observations, we split the analysis in two stages. In the first step, we evaluate the parameterizations of the self-collection process solely and, in the second step, we evaluate the parameterizations of the self-collection and breakup processes combined.

5.1 Self-Collection process

In order to facilitate the comparison between parameterizations and observations, the variations of N_r are studied as a function of D_{mv} only. This is achieved by dividing both terms of Equation 2 by N_r^2. Then, using the method described in Section 4, we can study the temporal variations of the total raindrop concentration dN_r/dt normalized by N_r^2 (called N_{var} hereafter; $N_{var} = (1/N_r^2)\,(dN_r/dt)$) as function of D_{mv}^3 using radar observations. The 2D histogram of N_{var} as function of D_{mv}^3 is very similar for both cases taken separately (Figure S3 in the supplementary material), suggesting that the overall behavior of the process is not case-dependent. Therefore, we combined the data from both case studies in Figure 8. To ease the interpretations, we superimpose the median values (and first (Q1) and third (Q3) quartiles) of N_{var} as function of D_{mv}^3. Most of the D_{mv}^3 data is ranging between 0.2 and 1.6 mm^3 (equivalent to D_{mv} ranging between 0.6 and 1.7 mm). N_{var} is mostly negative, i.e. representing a decrease of the number of raindrops as function of time, as expected in case of self-collection. N_{var} is close to zero for D_{mv}^3 lower than 0.6 mm^3 ($D_{mv} < 0.84$ mm) suggesting that collisions between raindrops are rare for such distributions of raindrops. For larger D_{mv}^3, N_{var} decreases in average towards values of around -3×10^{-6} m^3 s^{-1}.

It is not surprising to get a rather large dispersion of the data since these parameters are derived from remotely-sensed observations via a retrieval which necessarily implies some uncertainties. Starting from the uncertainty of the retrieved concentration for each diameter and each RSD provided by the variational method (via the covariance matrix of the solution described in Tridon et al., 2015), we have calculated how the uncertainty of the radar retrieval propagates through the successive computational steps in the Appendix A. The computation of the difference in raindrop concentration (Equation 10) leads to the biggest increase in relative error since it provides a small quantity from two parameters associated with a non-negligible uncertainty. The resulting uncertainty in N_{var} for a single radar pixel is shown as the gray error bars in Figure 8 for three different diameters. Interestingly, the error bars have a size similar to the Q1/Q3 range, suggesting that most of the dispersion can be explained by the uncertainty in the radar retrieval (in a specific *ad hoc* study in the Appendix B, we also showed that the uncertainty in the horizontal wind profile has a negligible impact on the results). This is further confirmed by the fact that the retrieval uncertainty increases with D_{mv}^3 exactly like the dispersion of the data. Even if the dispersion is large, a statistically significant mean behavior of N_{var} can be derived provided that

enough independent observations are available as it is the case with our dataset (at least 1,000 N_{var} estimates per D_{mv} bin).

On top of the observations shown in Figure 8, we superimpose the parameterizations of Ziegler (1985) (Z85; in purple), Seifert (2008) (S08; in orange) and Morrison et al. (2012) (Morr-CTL; same as Z85). These parameterizations result in a simple linear fit between N_{var} and D_{mv}^3. The only difference among them is a steeper slope for S08. Overall, all these parameterizations seem to significantly overestimate the effect of self-collection, even for small D_{mv}^3 where breakup can be considered negligible.

A simple linear fit (i.e., as function of D_{mv}^3) can better match the overall trend of the median of N_{var} when using a different slope (red dashed line). However, it seems to underestimate N_{var} for D_{mv}^3 ranging between 0-0.7 mm^3 and to overestimate N_{var} for D_{mv}^3 ranging between 0.7-1.4 mm^3. Indeed, up to 1 mm^3, the trend of the median of N_{var} seems to vary proportionally to 1/X² (i.e., proportionally to $1/D_{mv}^6$) and becomes linear only for larger D_{mv}^3. This might indicate two different regimes with self-collection only for small D_{mv}^3 and a combination of self-collection and breakup for larger D_{mv}^3. As a result, Figure 8 also shows the fit in $1/D_{mv}^6$ of the median of N_{var} up to 1 mm^3 (red solid line), corresponding to the following expression (analogously to Wood (2006) but defined for small diameters, see Equation 2):

$$\frac{dN_r}{dt} = -b\, N_r^2\, D_{mv}^6\, E_c \qquad \text{(Equation 13)}$$

with $b = 2.06 \times 10^{12}$ m^{-3}s^{-1}, D_{mv}^6 in mm^6 and E_c the rain self-collection efficiency which is assumed equal to 1 for the time being because only the self-collection process is considered.

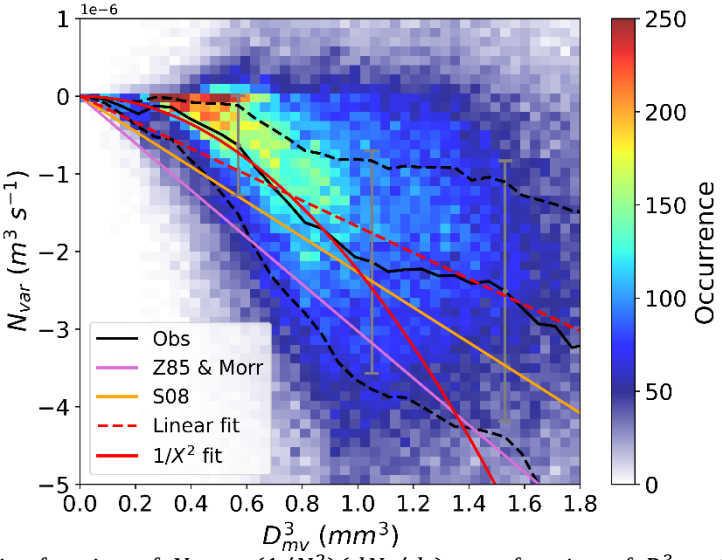

Figure 8 Probability density function of $N_{var} = (1/N_r^2)(dN_r/dt)$ as a function of D_{mv}^3 with observation points corresponding to the combination of the Finland and Oklahoma cases shown as a density plot in color. The median of observations per bin of diameter is represented by the black solid line and the first (Q1) and third (Q3) quartiles are represented by the black dashed lines. The error bars in gray represent the uncertainty of N_{var} for a single radar pixel. The parameterization of the self-collection process only (i.e. with E_c parameter set equal to 1) of Ziegler (1985) and Morrison et al. (2012) (Z85 & Morr) is shown in purple and, the one of Seifert (2008) (S08) in orange. The linear fit of the median of observations is shown by the red dashed line and the fit in $1/X^2$ (i.e. the final parameterization) by the continuous red line.

This newly-developed expression of the self-collection process (Equation 13) has been determined using a combination of the observation data from the two different case studies

described in Section 3. We made the same analysis by considering the observation data of each case independently (Figure S3) in order to verify the generality of our results. Table 1 summarizes the values obtained for the constant *b* and shows that they are fairly identical regardless of the case study used.

Observational data	b (m^{-3} s^{-1})	a (mm^{-1})	$D_{mv,th}$ (mm)
Oklahoma	2.31×10^{12}	2.55	0.94
Finland	2.19×10^{12}	3.87	0.97
Oklahoma & Finland	2.24×10^{12}	3.37	0.96

Table 1. Values obtained for the constant *b* (in m^{-3} s^{-1}) used in Equation 13 and for the constant *a* (in mm^{-1}) and $D_{mv,th}$ (in mm) used in Equation 14 considering the observation data from the Oklahoma case, the Finland case or using the combination of both case studies.

5.2 Self-Collection and breakup processes

In Section 5.1, only the self-collection process is considered (i.e. the rain self-collection efficiency E_c was assumed to be equal to 1 in Equation 13; see also Section 2) and an expression for E_c is now determined to study the effect of the breakup process. Indeed, once the constant b has been determined, Equation 13 can be re-arranged to derive E_c from N_r, $\frac{dN_r}{dt}$ and D_{mv} parameters.

Figure 9 presents the computed values of E_c from the retrieved parameters as function of D_{mv} as in Figure 1. E_c values are computed for D_{mv} ranging between 0.75 and 1.50 mm which corresponds to the size range of the observation data when combining the Oklahoma and Finland cases. Note that such size range is very close to that of Williams et al. (2014), who used a large dataset of disdrometer observations in various rain conditions, with a D_{mv} ranging from 0.35 to 1.76 mm (equivalent to a D_m ranging from 0.5 to 2.5 mm). Like for Figure 8, error bars corresponding to the uncertainty of *Ec* for a single radar pixel are shown in gray. They are also in agreement with the dispersion of the data: the error bars are larger for the smallest diameters where dispersion is the greatest. Therefore, the values of E_c greater than 1 are within the error interval and can be explained by the uncertainty of the radar retrieval. Figure 9 shows that for D_{mv} larger than 1 mm, E_c values are in average positive and lower than 1 which indicates that the self-collection and breakup processes occur simultaneously and that the self-collection process is dominating for most of the dataset (see Section 2.2). The variation of the median of E_c as function of D_{mv} (black solid line) exhibits an exponential decrease similar to Ziegler (1985) (Equation 4) but starting at a D_{mv} of 0.96 mm instead of 0.6 mm (see Figure 1). Thus, according to the observations, the effect of the breakup process seems to become visible in the observations for mean volume raindrop sizes slightly larger than what was predicted by Ziegler (1985). The fit of the median of E_c is shown in Figure 9 (red solid line) and leads to the following parameterization:

$$E_c = \begin{cases} 1, & D_{mv} < D_{mv,th} \\ \exp[-a\,(D_{mv} - D_{mv,th})], & D_{mv} \geq D_{mv,th} \end{cases} \quad \text{(Equation 14)}$$

with a = 3.14 mm^{-1}, D_{mv} in mm and the threshold mean volume diameter $D_{mv,th}$ = 0.96 mm.

As in Section 5.1, we carried out this study considering three different observational datasets (i.e. data from the Oklahoma case, from the Finland case, and from the combination of both cases, see Figure S3). In these three different situations, the variation of E_c according to D_{mv}

can be expressed by Equation 14 with values for a and $D_{\mathrm{mv,th}}$, as listed in Table 1. We observe a difference in the parameter a between the two cases, this parameter impacts the slope of the final parameterization (Figure 10 for both cases and Figure S3 for each case taken separately) for $D_{mv}{}^3 > 1.5$ mm^3. This suggests that our parameterization is slightly more uncertain for this range of D_{mv} which are not the most frequently observed.

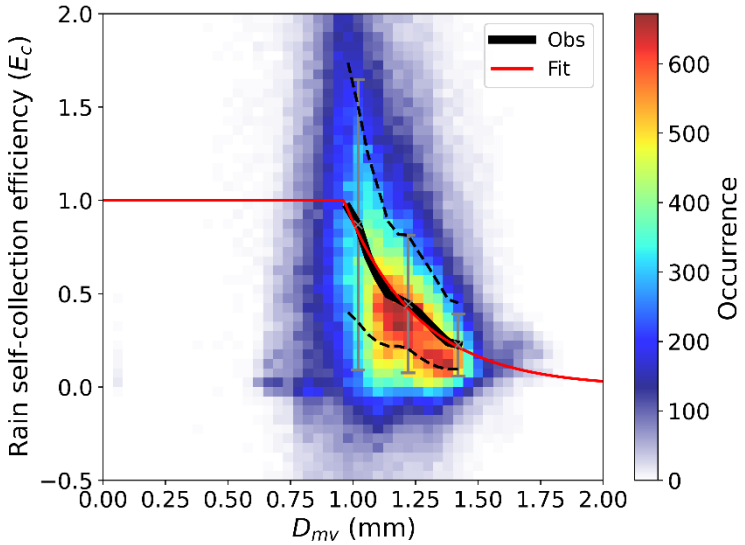

Figure 9. Probability density function of the rain self-collection efficiency (E_c) as a function of D_{mv} with observation points corresponding to the combination of the Finland and Oklahoma cases shown as a density plot in color. The median of the observations is represented by the black solid line while the first (Q1) and third (Q3) quartiles are represented by the black dashed lines. The error bars in gray represent the uncertainty of E_c for a single radar pixel. The exponential fit of the median of observations is shown by the red solid line (see Equation 14).

The combination of Equation 13 and Equation 14 provides a new parameterization for the self-collection and breakup processes, illustrated in Figure 10 (which is a zoom out of Figure 8). It can be compared to the parameterizations (described in Section 2) which are currently used in two-moment bulk microphysics schemes. Thus, Figure 10 also shows the values of N_{var} as a function of D_{mv}^3 for all the aforementioned parameterizations (Section 2.1), using for each of them the appropriate expression of E_c (see Section 2.2). For clarification, we remind that, in Figure 8, E_c was set equal to 1 to study the self-collection process only (Figure 8).

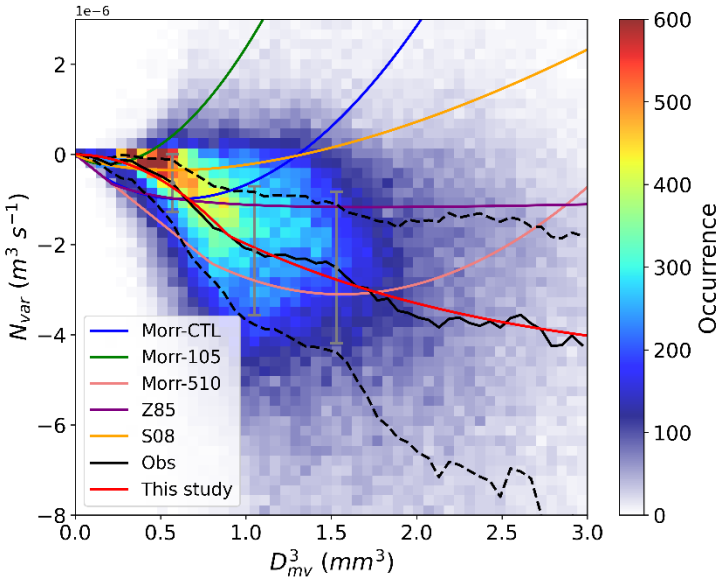

Figure 10 Probability density function of $N_{\mathrm{var}} = (1/N_{\mathrm{r}}^2)(dN_{\mathrm{r}}/dt)$ as a function of D^3_{mv} with observation points corresponding to the combination of the Finland and Oklahoma cases shown as a density plot in color. The median of the observations per bin of diameter is represented by the black solid line and the first (Q1) and third (Q3) quartiles are represented by the black dashed lines. The error bars in gray represent the uncertainty N_{var} for a single radar pixel. The parameterization of the self-collection and breakup processes (i.e. with E_{c} parameter following the expressions given in Section 2.2) of Ziegler (1985) (Z85) Morrison et al. (2012) (Morr-CTL, Morr-105 and Morr-510) and Seifert (2008) (S08) are shown by the purple, blue, green, pink and orange lines, respectively. The parameterization developed in this study is represented in red.

As expected, Figure 10 shows that the parameterization developed in this study follows the trend deduced from the multifrequency radar observations. Up to $D_{\mathrm{mv}} = 0.96$ mm ($D^3_{mv} = 0.88\ mm^3$), N_{var} follows the $1/D^6_{\mathrm{mv}}$ trend derived in Section 5.1. Above this threshold, the breakup becomes more and more efficient (as suggested by Equation 14) and N_{var} decreases at a slower rate. However, the effect of breakup seems to never be efficient enough to counteract the effect of collection. This results in a continuous decrease of N_{var} from 0 to -4×10^{-6} m^3 s^{-1} for D^3_{mv} ranging from 0 to 3 mm^3 (equivalent to D_{mv} ranging from 0 to 1.4 mm). Hence, these negative values indicate that the self-collection process is more efficient than the breakup process over the whole size range in which observations are in sufficient quantity to provide a trend with high confidence (i.e. to D_{mv} ranging between 0.67 and 1.26 mm). Note that for larger D_{mv}, the tendency is determined with low confidence and is mainly driven by the expression chosen for E_{c} (Equation 14) which is good fit of the data up to 1.5 mm. For larger D_{mv}, observations from more cases with exceptionally large drops would be necessary to confirm the limited effect of breakup with respect to collection.

Figure 10 also compares the parameterizations of Z85, Morr-CTL and S08 (and the other versions tested in Morrison et al. (2012), i.e. Morr-105 and Morr-510). Interestingly, they are all in the same ballpark as the observations, but their size dependency differs strongly. On one hand, Morr-105, Morr-CTL and S08 seem to overestimate the breakup effect, with N_{var} becoming positive for D^3_{mv} larger than 0.4, 1.3 and 1.2 mm^3, respectively (i.e. D_{mv} larger than 0.74, 1.09 and 1.06 mm). Thus, for raindrops larger than these D^3_{mv}, N_{var} increases as function of time, i.e. implying a dominating effect of breakup with respect to self-collection. Nevertheless, for smaller

D_{mv}^3, Morr-105 and S08 are rather close to the observations while Morr-CTL suggests a too strong self-collection process. On the other hand, Z85 and Morr-510 are within the range of the observations (within the Q1-Q3 range) except for the smallest raindrops. When comparing to the median of the observations, the N_{var} resulting from Morr-510 appears too small for D_{mv}^3 smaller than 1.8 mm^3 (i.e. over the whole size range in which observations are in sufficient quantity to provide a trend with high confidence) suggesting an overestimated dominating effect of self-collection. In the case of Z85, N_{var} is underestimated and overestimated for D_{mv}^3 smaller and larger than 0.7 mm^3, respectively. Thus, even if results obtained with Z85 diverge over the whole size range, in average, it is the representation of the self-collection and breakup processes which provides the closest results to the new parameterization derived in this study.

6 Conclusions

The self-collection (or collision-coalescence) and breakup of raindrops are key processes impacting the population of falling raindrops but they are still poorly represented in models using two-moment bulk microphysics schemes (Morrison et al., 2020). Both of these processes are generally described by a single expression providing the temporal evolution of the raindrop concentration (dN_{r}/dt) as function of raindrop properties (e.g. mean volume diameter D_{mv} and total number concentration N_{r}) and rain self-collection efficiency (E_c) which is parameterized. All of these parameterizations were developed on the base of few laboratory experiments or from bin models (Low & List, 1982; Verlinde & Cotton, 1993; Seifert, 2008). However, as highlighted in this work, the resulting versions of the parameterizations used to describe the self-collection and breakup processes are significantly different, especially in their representation of the E_c parameter (Ziegler, 1985; Seifert, 2008; Morrison et al., 2012).

The multifrequency radar retrieval technique developed by Tridon and Battaglia (2015) and Tridon et al. (2019b) (combining the observations from K_a- and W-band radars) allows to retrieve binned RSDs (raindrop size distributions) with high temporal and vertical resolutions. This enabled us to study the temporal evolution of the vertical profiles of the RSDs and corresponding parameters such as D_{mv}, N_{r} and RWC, and then to evaluate the parameterizations of raindrop self-collection and breakup processes using observations of natural clouds and precipitation. In contrast to previous studies where parameterizations were evaluated using disdrometers located at the surface (as in Morrison et al., 2012; Saleeby et al., 2022; among others), the radar retrieved rain properties allowed to perform this evaluation through the entire precipitating layer. In this framework, an analysis method has been developed to study the variations of dN_{r}/dt and E_c. A key element of this method is to use the approach of Hogan and Kew (2005) for extracting the spatiotemporal variations of raindrop properties along their respective trajectories which depend on their size and on the wind properties (vertical wind and wind shear).

The analysis method was applied to two cases with different properties: a mid-latitude stratiform precipitation event observed on 7 June 2014 at Hyytiälä in Finland (Tridon et al., 2017a) and the transition and stratiform regions of a squall-line system observed on 12 June 2011 at the SGP (Southern Great Plains) site in Oklahoma (Tridon et al., 2019b). The convective region of the squall line was excluded because the signal of the radars, especially the W-band radar, are heavily attenuated by strong rainfall (Tridon & Battaglia, 2015; Tridon et al., 2019b). These two cases benefited of the facilities of the U.S. DOE ARM program (Petäjä et al., 2016; Kollias et al., 2020) where K_a- and W-band radars were co-localized. Unfortunately, such experimental design is very rarely set up for rain observations (i.e. it is most often used for high latitude sites, and profiling

observations are generally made only intermittently), thus there is little availability of data for reproducing this work on more numerous case studies. Nevertheless, the two case studies complement each other rather well and show very similar trends in the size range where uncertainties are low.

Our results show that even if the current parameterizations for raindrop self-collection and breakup processes produce variations in raindrop concentration which are in the same ballpark as the observations, they diverge from the median of the observations implying an overestimation of either the self-collection or the breakup process depending on the raindrop size. Morr-105, Morr-CTL and S08 overestimate the breakup process for D_{mv} larger than 0.74, 1.09 and 1.06 mm while Morr-510 overestimates the self-collection process over the entire observed size range. Z85 overestimates the self-collection process for D_{mv} smaller than 0.9 mm and overestimates the breakup process for larger raindrops but remains within the observed range of variability. By fitting the median of the variations in raindrop concentration obtained from radar observations, we developed a new parameterization to describe the combined effect of the self-collection and breakup processes: (*i*) by adapting an expression given in Wood (2006) to represent the rate of raindrop concentration (dN_{r}/dt) (Equation 13) and (*ii*) by representing the self-collection efficiency (E_{c}) with the mathematical form of Ziegler (1985) (Equation 14), which was the closest to the observations.

In future work, the new parameterization of the raindrop self-collection and breakup processes will be implemented in a two-moment bulk microphysics scheme in order to quantify the influence of raindrop microphysics on the overall precipitation systems, via bulk evaporation rates and hence cold pool characteristics, and on ice formation via ascendances of small raindrops toward negative temperature in convective systems. Furthermore, since the multifrequency radar retrieval provides binned RSDs, it could also be exploited to study the self-collection and breakup processes in models using a bin microphysics scheme such as DESCAM (Detailed scavenging model; Flossmann & Wobrock, 2010; Planche et al., 2010, 2014) or HUCM (Hebrew University Cloud Model; Khain et al., 2004).

Appendix A: Calculation of the radar retrieval uncertainty propagation to the process rate estimate

The radar retrieval provides the uncertainty (standard deviation) of the retrieved concentration ΔN_D for each diameter *D*. The first step in the method described in Section 4 is to determine the vertical variation of the concentration dN_D/dz (Equation 10). To calculate the propagation of uncertainties, we make the quadratic sum of the standard deviation of each sources of uncertainty, assuming no correlation between them. Thus, the uncertainty of dN_D/dz is:

$$\Delta\left(\frac{dN_D}{dz}(z_k)\right) = \frac{\sqrt{\Delta N_D\left(t_D(z_{k+1})\right)^2 + \Delta N_D\left(t_D(z_{k-1})\right)^2}}{z_{k+1} - z_{k-1}} \qquad \text{(Equation A1)}$$

where we assume that the error in the trajectory of the raindrops is negligible following the analysis of the Appendix B. Then, the uncertainty of the temporal variation of the concentration along the raindrop trajectory dN_D/dt (Equation 11) is:

$$\Delta\left(\frac{dN_D}{dt}(z_k)\right) = \sqrt{\left(\left(V_{t,D}(z_k) - w(z_k)\right)\Delta\left(\frac{dN_D}{dz}(z_k)\right)\right)^2 + \left(\frac{dN_D}{dz}(z_k)\,\Delta V_{t,D}(z_k)\right)^2 + \left(\frac{dN_D}{dz}(z_k)\,\Delta w(z_k)\right)^2}$$

(Equation A2)

Where we set $\Delta V_{t,D}(z_k) = 1\ m\ s^{-1}$ based on the Figure 3 from Raupach and Berne (2015) and where $\Delta w(z_k)$ is provided by the radar retrieval (of the order of 0.06 m s^{-1}).

The next step is to compute the temporal variation of the total concentration of raindrops dN_r/dt (Equation 12), its uncertainty is calculated as follows:

$$\Delta\left(\frac{dN_r}{dt}(z_k)\right) = \sqrt{\sum_{D_i}\Delta\left(\frac{dN_{D_i}}{dt}(z_k)\right)^2} \quad \text{(Equation A3)}$$

The uncertainty of the N_{var} variable (shown in Figures 8 and 10) is:

$$\Delta N_{var} = |N_{var}|\sqrt{2\left(\frac{\Delta N_r}{N_r}\right)^2 + \left(\frac{\Delta dN_r/dt}{dN_r/dt}\right)^2} \quad \text{(Equation A4)}$$

with:

$$\Delta N_r = \sqrt{\Sigma_{D_i} N_{D_i}^2} \quad \text{(Equation A5)}$$

For the rain self-collection efficiency E_c derived from observations and deduced from Equation 13, its associated uncertainty is calculated as follows:

$$\Delta E_c = |E_c|\sqrt{\left(\frac{\Delta dN_r/dt}{dN_r/dt}\right)^2 + 2\left(\frac{\Delta N_r}{N_r}\right)^2 + 6\left(\frac{\Delta D_{mv}}{D_{mv}}\right)^2} \quad \text{(Equation A6)}$$

where:

$$\Delta D_{mv} = \frac{1}{3}|D_{mv}|\left(\frac{\Delta M_3}{M_3} + \frac{\Delta N_r}{N_r}\right) \quad \text{(Equation A7)}$$

The resulting approximate relative errors at each step described above (for an altitude of 1 km and two diameters 0.6 and 3 mm) are presented in Table A1. This shows that the relative error starts from relatively low values for the raindrop concentration of the RSD (35% for 0.6 mm and 25% for 3 mm). The biggest increase in relative error comes from the computation of *dN/dt* (*dN/dz* is not included in the table since its values is identical). Moreover, uncertainty is higher for small diameters (80% for 0.6 mm) and decreases with increasing diameters (50% for 3 mm). The relative error of dN_r/dt is 80%, which is consistent with the maximum error of *dN/dt*. The error of N_r and D_{mv} is quite small, of the order of 15% and 6%, respectively. Therefore, these parameters have little impact on the calculation of the uncertainty of N_{var} and E_c, whose relative errors are of the order of 80% and 90%, respectively.

Relative error (in %)	$\frac{\Delta N}{N}$	$\frac{\Delta\, dN/dt}{dN/dt}$	$\frac{\Delta\, dN_r/dt}{dN_r/dt}$	$\frac{\Delta N_r}{N_r}$	$\frac{\Delta D_{mv}}{D_{mv}}$	$\frac{\Delta N_{var}}{N_{var}}$	$\frac{\Delta E_c}{E_c}$
D = 0.6 mm	35	80	80	15	6	80	90
D= 3 mm	25	50					

Table A1. Approximate relative error obtained at an altitude of 1 km and for two diameters (0.6 and 3 mm) for each step of the analysis method.

Appendix B: Contribution from the uncertainty in the horizontal wind profile

In Section 4, Equation 7 describes a numerical approach to compute iteratively the horizontal displacement of a drop as it falls from a reference level by taking into account its fall velocity and the profile of horizontal and vertical wind. The vertical wind and the fall velocity (via the determination of the raindrop size) are provided with relatively good accuracy by the radar retrieval. On the contrary, the profile of the horizontal wind can only be derived from the closest radiosonde in time, i.e. with relatively high uncertainty. Hence, it is important to evaluate the impact of the horizontal wind uncertainty on the determination of the raindrop trajectory.

Equation 7 derives from a more general analytical equation (following Hogan & Kew, 2005) that we rewrite in a simplified form involving only the horizontal winds at the surface u_0 and at the reference level u_{ref}:

$$\frac{\delta x}{\delta z} = \frac{u_0 - u_{ref}}{v_t} \quad \text{(Equation B1)}$$

where δx is the horizontal displacement of the drop as it falls through the layer δz from the reference level to the surface and v_t is its fall speed. Using Equation 9, we can convert it to the trajectory in the time-height space of the radar observations:

$$\frac{\delta t}{\delta z} = \frac{u_0 - u_{ref}}{v_t\, u_{ref}} \quad \text{(Equation B2)}$$

Noting that the horizontal wind at the surface tends towards zero, it is convenient to replace the unknown wind at the reference level u_{ref} by the magnitude of the horizontal wind shear δu (i.e., difference between winds at the surface and at the reference level $\delta u = u_0 - u_{ref}$):

$$\frac{\delta t}{\delta z} = \frac{\delta u}{v_t(u_0 - \delta u)} \quad \text{(Equation B3)}$$

The trajectory time difference between the reference level and the surface (i.e. the time difference at which the drop will be sampled by the radar at these levels) is therefore:

$$\delta t = \frac{\delta z}{v_t\left(\frac{u_0}{\delta u} - 1\right)} \quad \text{(Equation B4)}$$

From this equation, we can study how an uncertainty in the horizontal wind shear $\Delta\delta u$ propagates in an uncertainty in the trajectory time difference $\Delta\delta t$, as function of the wind at the surface u_0. For this experiment, we set the thickness of the layer to $\delta z = 2\ km$ and the fall velocity to $v_t = 4\ m\ s^{-1}$ (corresponding to a drop of 1 mm). We computed the relative error in the trajectory time difference $\Delta(\delta t)/\delta t$ as function of the relative error in the horizontal wind shear $\Delta(\delta u)/\delta u$ (where $\Delta(\delta u) = \widehat{\delta u} - \delta u$ with $\widehat{\delta u}$ the estimated value of the wind shear), starting from three different values of δu: 10 m s^{-1} (Figure B1a), 16 m s^{-1} (Figure B1b) and 25 m s^{-1} (Figure B1c). In these figures, the colors of the curves corresponds to different winds at the surface u_0 from 0 to 2 m s^{-1} (the latter being a rather high value for surface wind). These figures show that the relative error $\Delta(\delta u)/\delta u$ always results in smaller relative error in $\Delta(\delta t)/\delta t$, with e.g. a maximum $\Delta(\delta t)/\delta t$ of around 10% and 30% for $u_0 = 1\ m\ s^{-1}$ and $2\ m\ s^{-1}$, respectively. But more importantly, when u_0 is lower than 0.5 m s^{-1} (as it is usually the case near the surface) the relative error $\Delta(\delta t)/\delta t$ becomes negligible (e.g. less than 3% for $u_0 = 0.2\ m\ s^{-1}$) and the magnitude of the horizontal wind shear δu becomes insignificant. In conclusion, when focusing on near-surface data, this study suggests that the profile of the horizontal wind has little effect in determining the trajectory of the drops and hence, that it is enough to use the measurement from a nearby radiosonde. The fact that the propagation of the radar retrieval errors is enough to explain the dispersion of our data in Figures 9 and 10 confirms that the uncertainty in the horizontal wind profile is of secondary importance.

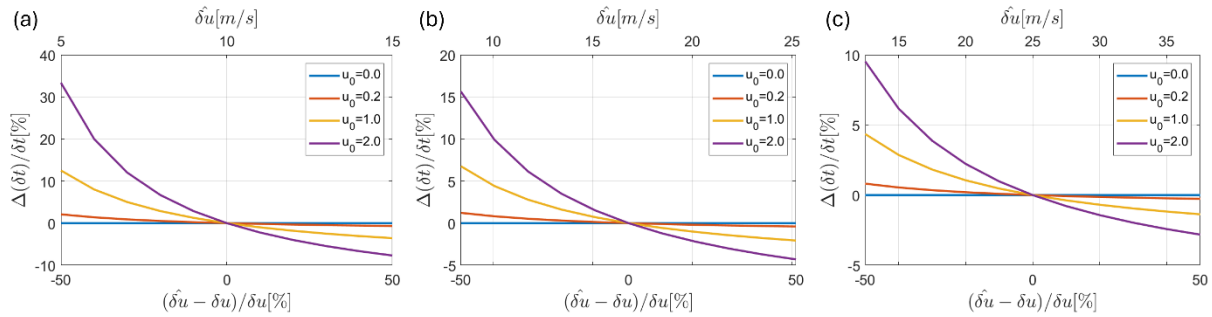

Figure B1. Relative error of the trajectory time difference $\Delta(\delta t)/\delta t$ of a drop of 1 mm falling though a layer of 2 km as function of the relative error in the horizontal wind shear $\Delta(\delta u)/\delta u$ (where $\Delta(\delta u) = \widehat{\delta u} - \delta u$), using three different values of δu: 10 m s^{-1} (a), 16 m s^{-1} (b) and 25 m s^{-1} (c) and four different values of u_0: 0 m s^{-1} (blue), 0.2 m s^{-1} (orange), 1 m s^{-1} (yellow) and 2 m s^{-1} (purple).

Acknowledgments

The authors declare no conflict of interest. The lead author is funded by a doctoral fellowship from the Doctoral School of the Fundamental Sciences (EDSF) of the University Clermont Auvergne (UCA). This work is a contribution to the ACME project, supported by the Agence Nationale de la Recherche under the Grant ANR-21-CE01-0003. The authors acknowledge all the persons involved in the ARM program for supplying the data used in this study. L.N. would also like to acknowledge Axel Seifert for the details he provided about the development of his parameterizations on raindrop self-collection/breakup processes.

Open Research

Radar data were obtained from the U.S. DOE Atmospheric Research Measurement (ARM) Climate Research Facility:

- For Finland case:
  - K_a-band ARM Zenith Radar (KAZR) provided by ARM user facility (2014a);
  - W-band ARM cloud radar (MWACR) provided by ARM user facility (2014b)
- For Oklahoma case:
  - Radar Wind Profiler (RWP) provided by ARM user facility (1998);
  - K_a-band ARM Zenith Radar (KAZR) provided by ARM user facility (2011a);
  - W-band ARM cloud radar (WSACR) provided by ARM user facility (2011b).

The radar retrieval data used in this study is provided by Niquet et al. (2024).

References

Atlas, D., Srivastava, R. C., & Sekhon, R. S. (1973). Doppler radar characteristics of precipitation at vertical incidence. *Reviews of Geophysics*, *11*(1), 1-35. https://doi.org/10.1029/RG011i001p00001

Atmospheric Radiation Measurement (ARM) user facility. 1998. Radar Wind Profiler (915RWPPRECIPMOM). 2011-06-12 to 2011-06-12, Southern Great Plains (SGP) Central Facility, Lamont, OK (C1). Compiled by R. Coulter, P. Muradyan and T. Martin. ARM Data Center. Data set accessed 2023-08-28 at http://dx.doi.org/10.5439/1993147.

Atmospheric Radiation Measurement (ARM) user facility. 2011a. Ka ARM Zenith Radar (KAZRGE). 2011-06-12 to 2011-06-12, Southern Great Plains (SGP) Central Facility, Lamont, OK (C1). Compiled by I. Lindenmaier, Y. Feng, K. Johnson, A. Matthews, T. Wendler, V. Castro, M. Deng and M. Rocque. ARM Data Center. Data set accessed 2023-08-28 at http://dx.doi.org/10.5439/1984770.

Atmospheric Radiation Measurement (ARM) user facility. 2011b. W-band Scanning ARM Cloud Radar (WSACRVPT). 2011-06-11 to 2011-06-13, Southern Great Plains (SGP) Central Facility, Lamont, OK (C1). Compiled by I. Lindenmaier, Y. Feng, K. Johnson, A. Matthews, T. Wendler, V. Castro, M. Deng and M. Rocque. ARM Data Center. Data set accessed 2023-08-28 at http://dx.doi.org/10.5439/1984008.

Atmospheric Radiation Measurement (ARM) user facility. 2014a. Ka ARM Zenith Radar (KAZRGE). 2014-06-07 to 2014-06-07, ARM Mobile Facility (TMP) U. of Helsinki Research Station (SMEAR II), Hyytiala, Finland; AMF2 (M1). Compiled by I. Lindenmaier, Y. Feng, K. Johnson, A. Matthews, T. Wendler, V. Castro and M. Deng. ARM Data Center. Data set accessed 2023-06-30 at http://dx.doi.org/10.5439/1984772.

Atmospheric Radiation Measurement (ARM) user facility. 2014b. Marine W-Band (95 GHz) ARM Cloud Radar (MWACR). 2014-06-07 to 2014-06-07, ARM Mobile Facility (TMP) U. of Helsinki Research Station (SMEAR II), Hyytiala, Finland; AMF2 (M1). Compiled by I. Lindenmaier, K. Johnson, A. Matthews, T. Wendler, V. Castro and M. Deng. ARM Data Center. Data set accessed 2023-06-30 at http://dx.doi.org/10.5439/1973911.

Barthes, L., & Mallet, C. (2013). Vertical evolution of raindrop size distribution: Impact on the shape of the DSD. *Atmospheric Research*, *119*, 13-22. https://doi.org/10.1016/j.atmosres.2011.07.011

Beard, K. V., & Ochs , H. T., III. (1995). Collisions between Small Precipitation Drops. Part II: Formulas for Coalescence, Temporary Coalescence, and Satellites. *Journal of Atmospheric Sciences*, *52*(22), 3977-3996. https://doi.org/10.1175/1520-0469(1995)052<3977:CBSPDP>2.0.CO;2

Beheng, K. D. (1994). A parameterization of warm cloud microphysical conversion processes. *Atmospheric Research*, *33*(1-4), 193-206. https://doi.org/10.1016/0169-8095(94)90020-5

Berry, E. X. (1967). Cloud Droplet Growth by Collection. *Journal of Atmospheric Sciences*, *24*(6), 688-701. https://doi.org/10.1175/1520-0469(1967)024<0688:CDGBC>2.0.CO;2

Berry, E. X., & Reinhardt, R. L. (1974). An Analysis of Cloud Drop Growth by Collection: Part I. Double Distributions. *Journal of Atmospheric Sciences*, *31*(7), 1814-1824. https://doi.org/10.1175/1520-0469(1974)031<1814:AAOCDG>2.0.CO;2

Billault-Roux, A. C., Georgakaki, P., Gehring, J., Jaffeux, L., Schwarzenboeck, A., Coutris, P., ... & Berne, A. (2023). Distinct secondary ice production processes observed in radar Doppler spectra: insights from a case study. *Atmospheric Chemistry and Physics*, *23*(17), 10207-10234. https://doi.org/10.5194/acp-23-10207-2023

Bleck, R. (1970). A fast, approximative method for integrating the stochastic coalescence equation. *Journal of Geophysical Research*, *75*(27), 5165-5171. https://doi.org/10.1029/JC075i027p05165

Bott, A. (1998). A Flux Method for the Numerical Solution of the Stochastic Collection Equation. *Journal of the Atmospheric Sciences*, *55*(13), 2284-2293. https://doi.org/10.1175/1520-0469(1998)055<2284:AFMFTN>2.0.CO;2

Brazier-Smith, P. R., Jennings, S. G., & Latham, J. (1972). The interaction of falling water drops: coalescence. *Proceedings of the Royal Society of London. A. Mathematical and Physical Sciences*, *326*(1566), 393-408. https://doi.org/10.1098/rspa.1972.0016

Brown, P. S., Jr. (1993). Analysis and Parameterization of the Combined Coalescence, Breakup, and Evaporation Processes. *Journal of Atmospheric Sciences*, *50*(17), 2940-2951. https://doi.org/10.1175/1520-0469(1993)050<2940:AAPOTC>2.0.CO;2

Flossmann, A. I., & Wobrock, W. (2010). A review of our understanding of the aerosol–cloud interaction from the perspective of a bin resolved cloud scale modelling. *Atmospheric Research*, *97*(4), 478-497. https://doi.org/10.1016/j.atmosres.2010.05.008

Frisch, A. S. , Fairall, C. W. , & Snider, J. B. . (1995). Measurement of Stratus Cloud and Drizzle Parameters in ASTEX with a Kα-Band Doppler Radar and a Microwave Radiometer. *Journal of Atmospheric Sciences*, *52*(16), 2788-2799. https://doi.org/10.1175/1520-0469(1995)052<2788:MOSCAD>2.0.CO;2

Gelbard, F., & Seinfeld, J. H. (1978). Numerical solution of the dynamic equation for particulate systems. *Journal of Computational Physics*, *28*(3), 357-375. https://doi.org/10.1016/0021-9991(78)90058-X

Grzegorczyk, P., Yadav, S., Zanger, F., Theis, A., Mitra, S. K., Borrmann, S., & Szakáll, M. (2023). Fragmentation of ice particles: laboratory experiments on graupel-graupel and graupel-snowflake collisions. *EGUsphere*, *2023*, 1-31. https://doi.org/10.5194/egusphere-2023-1074

Hogan, R. J., & Kew, S. F. (2005). A 3D stochastic cloud model for investigating the radiative properties of inhomogeneous cirrus clouds. *Quarterly Journal of the Royal Meteorological Society: A journal of the atmospheric sciences, applied meteorology and physical oceanography*, *131*(611), 2585-2608. https://doi.org/10.1256/qj.04.144

Hu, Z., & Srivastava, R. C. (1995). Evolution of Raindrop Size Distribution by Coalescence, Breakup, and Evaporation: Theory and Observations. *Journal of Atmospheric Sciences*, *52*(10), 1761-1783. https://doi.org/10.1175/1520-0469(1995)052<1761:EORSDB>2.0.CO;2

Kagkara, C., Wobrock, W., Planche, C., & Flossmann, A. I. (2020). The sensitivity of intense rainfall to aerosol particle loading–a comparison of bin-resolved microphysics modelling with observations of heavy precipitation from HyMeX IOP7a. *Natural Hazards and Earth System Sciences*, *20*(5), 1469-1483. https://doi.org/10.5194/nhess-20-1469-2020

Khain, A. P., Beheng, K. D., Heymsfield, A., Korolev, A., Krichak, S. O., Levin, Z., ... & Yano, J. I. (2015). Representation of microphysical processes in cloud-resolving models: Spectral (bin) microphysics versus bulk parameterization. *Reviews of Geophysics*, *53*(2), 247-322. https://doi.org/10.1002/2014RG000468

Khain, A., Pokrovsky, A., Pinsky, M., Seifert, A., & Phillips, V. (2004). Simulation of effects of atmospheric aerosols on deep turbulent convective clouds using a spectral microphysics mixed-phase cumulus cloud model. Part I: Model description and possible applications. *Journal of the atmospheric sciences*, *61*(24), 2963-2982. https://doi.org/10.1175/JAS-3350.1

Kollias, P., Bharadwaj, N., Clothiaux, E. E., Lamer, K., Oue, M., Hardin, J., Isom, B., Lindenmaier, I., Matthews, A., Luke, E. P., Giangrande, S. E., Johnson, K., Collis, S., Comstock, J., & Mather, J. H. (2020). The ARM Radar Network: At the Leading Edge of Cloud and Precipitation Observations. *Bulletin of the American Meteorological Society*, *101*(5), E588-E607. https://doi.org/10.1175/BAMS-D-18-0288.1

Kumjian, M. R., & Ryzhkov, A. V. (2010). The Impact of Evaporation on Polarimetric Characteristics of Rain: Theoretical Model and Practical Implications. *Journal of Applied Meteorology and Climatology*, *49*(6), 1247-1267. https://doi.org/10.1175/2010JAMC2243.1

Lac, C., Chaboureau, J. P., Masson, V., Pinty, J. P., Tulet, P., Escobar, J., ... & Wautelet, P. (2018). Overview of the Meso-NH model version 5.4 and its applications. *Geoscientific Model Development*, *11*(5), 1929-1969. https://doi.org/10.5194/gmd-11-1929-2018

Lafore, J. P., Stein, J., Asencio, N., Bougeault, P., Ducrocq, V., Duron, J., ... & Vilà-Guerau de Arellano, J. (1998, January). The Meso-NH atmospheric simulation system. Part I: Adiabatic formulation and control simulations. In *Annales geophysicae* (Vol. 16, No. 1, pp. 90-109). Göttingen, Germany: Springer Verlag. https://doi.org/10.1007/s00585-997-0090-6

Leinonen, J., Lebsock, M. D., Tanelli, S., Sy, O. O., Dolan, B., Chase, R. J., ... & Moisseev, D. (2018). Retrieval of snowflake microphysical properties from multifrequency radar observations. *Atmospheric Measurement Techniques*, *11*(10), 5471-5488. https://doi.org/10.5194/amt-11-5471-2018

List, R., & Whelpdale, D. M. (1969). A Preliminary Investigation of Factors Affecting the Coalescence of Colliding Water Drops. *Journal of Atmospheric Sciences*, *26*(2), 305-308. https://doi.org/10.1175/1520-0469(1969)026<0305:APIOFA>2.0.CO;2

List, R., MacNeil, C. F., & McTaggart-Cowan, J. D. (1970). Laboratory investigations of temporary collisions of raindrops. *Journal of Geophysical Research*, *75*(36), 7573-7580. https://doi.org/10.1029/JC075i036p07573

Long, A. B. (1974). Solutions to the Droplet Collection Equation for Polynomial Kernels. *Journal of Atmospheric Sciences*, *31*(4), 1040-1052. https://doi.org/10.1175/1520-0469(1974)031<1040:STTDCE>2.0.CO;2

Low, T. B. , & List, R. (1982a). Collision, Coalescence and Breakup of Raindrops. Part I: Experimentally Established Coalescence Efficiencies and Fragment Size Distributions in Breakup. *Journal of Atmospheric Sciences*, *39*(7), 1591-1606. https://doi.org/10.1175/1520-0469(1982)039<1591:CCABOR>2.0.CO;2

Low, T. B. , & List, R. (1982b). Collision, Coalescence and Breakup of Raindrops. Part II: Parameterization of Fragment Size Distributions. *Journal of Atmospheric Sciences*, *39*(7), 1607-1619. https://doi.org/10.1175/1520-0469(1982)039<1607:CCABOR>2.0.CO;2

Mansell, E. R. (2010). On Sedimentation and Advection in Multimoment Bulk Microphysics. *Journal of the Atmospheric Sciences*, *67*(9), 3084-3094. https://doi.org/10.1175/2010JAS3341.1

Mason, S. L., Chiu, C. J., Hogan, R. J., Moisseev, D., & Kneifel, S. (2018). Retrievals of riming and snow density from vertically pointing Doppler radars. *Journal of Geophysical Research: Atmospheres*, *123*(24), 13-807–13,834. https://doi.org/10.1029/2018JD028603

Mason, S. L., Chiu, J. C., Hogan, R. J., & Tian, L. (2017). Improved rain rate and drop size retrievals from airborne Doppler radar. *Atmospheric Chemistry and Physics*, *17*(18), 11567-11589. https://doi.org/10.5194/acp-17-11567-2017

McTaggart-Cowan, J. D., & List, R. (1975). Collision and breakup of water drops at terminal velocity. *Journal of the Atmospheric Sciences*, *32*(7), 1401-1411.

Morrison, H., & Milbrandt, J. (2011). Comparison of Two-Moment Bulk Microphysics Schemes in Idealized Supercell Thunderstorm Simulations. *Monthly Weather Review*, *139*(4), 1103-1130. https://doi.org/10.1175/2010MWR3433.1

Milbrandt, J. A., & McTaggart-Cowan, R. (2010). Sedimentation-Induced Errors in Bulk Microphysics Schemes. *Journal of the Atmospheric Sciences*, *67*(12), 3931-3948. https://doi.org/10.1175/2010JAS3541.1

Morrison, H., & Milbrandt, J. (2011). Comparison of Two-Moment Bulk Microphysics Schemes in Idealized Supercell Thunderstorm Simulations. *Monthly Weather Review*, *139*(4), 1103-1130. https://doi.org/10.1175/2010MWR3433.1

Morrison, H., Tessendorf, S. A., Ikeda, K., & Thompson, G. (2012). Sensitivity of a Simulated Midlatitude Squall Line to Parameterization of Raindrop Breakup. *Monthly Weather Review*, *140*(8), 2437-2460. https://doi.org/10.1175/MWR-D-11-00283.1

Morrison, H., Thompson, G., & Tatarskii, V. (2009). Impact of Cloud Microphysics on the Development of Trailing Stratiform Precipitation in a Simulated Squall Line: Comparison of One- and Two-Moment Schemes. *Monthly Weather Review*, *137*(3), 991-1007. https://doi.org/10.1175/2008MWR2556.1

Morrison, H., van Lier-Walqui, M., Fridlind, A. M., Grabowski, W. W., Harrington, J. Y., Hoose, C., ... & Xue, L. (2020). Confronting the challenge of modeling cloud and precipitation microphysics. *Journal of advances in modeling earth systems*, *12*(8), e2019MS001689. https://doi.org/10.1029/2019MS001689

Mróz, K., Battaglia, A., Kneifel, S., D'Adderio, L. P., & Dias Neto, J. (2020). Triple-frequency Doppler retrieval of characteristic raindrop size. *Earth and Space Science*, *7*(3), e2019EA000789. https://doi.org/10.1029/2019EA000789

Mroz, K., Battaglia, A., Nguyen, C., Heymsfield, A., Protat, A., & Wolde, M. (2021). Triple-frequency radar retrieval of microphysical properties of snow. *Atmospheric Measurement Techniques*, *14*(11), 7243-7254. https://doi.org/10.5194/amt-14-7243-2021

Niquet, L., Tridon, F., & Planche, C. (2024). Evaluation of the representation of raindrops self-collection and breakup processes in 2-moment bulk models using multifrequency radar retrievals [Data set]. OPGC, LaMP. https://doi.org/10.25519/1GB0-1C84

Paukert, M., Fan, J., Rasch, P. J., Morrison, H., Milbrandt, J. A., Shpund, J., & Khain, A. (2019). Three-moment representation of rain in a bulk microphysics model. *Journal of Advances in Modeling Earth Systems*, *11*(1), 257-277. https://doi.org/10.1029/2018MS001512

Petäjä, T., O'Connor, E. J., Moisseev, D., Sinclair, V. A., Manninen, A. J., Väänänen, R., von Lerber, A., Thornton, J. A., Nicoll, K., Petersen, W., Chandrasekar, V., Smith, J. N., Winkler, P. M., Krüger, O., Hakola, H., Timonen, H., Brus, D., Laurila, T., Asmi, E., Riekkola, M., Mona, L., Massoli, P., Engelmann, R., Komppula, M., Wang, J., Kuang, C., Bäck, J., Virtanen, A., Levula, J., Ritsche, M., & Hickmon, N. (2016). BAECC: A Field Campaign to Elucidate the Impact of Biogenic Aerosols on Clouds and Climate. *Bulletin of the American Meteorological Society*, *97*(10), 1909-1928. https://doi.org/10.1175/BAMS-D-14-00199.1

Planche, C., Tridon, F., Banson, S., Thompson, G., Monier, M., Battaglia, A., & Wobrock, W. (2019). On the Realism of the Rain Microphysics Representation of a Squall Line in the WRF Model. Part II: Sensitivity Studies on the Rain Drop Size Distributions. *Monthly Weather Review*, *147*(8), 2811-2825. https://doi.org/10.1175/MWR-D-18-0019.1

Planche, C., Wobrock, W., & Flossmann, A. I. (2014). The continuous melting process in a cloud-scale model using a bin microphysics scheme. *Quarterly Journal of the Royal Meteorological Society*, *140*(683), 1986-1996. https://doi.org/10.1002/qj.2265

Planche, C., Wobrock, W., Flossmann, A. I., Tridon, F., Van Baelen, J., Pointin, Y., & Hagen, M. (2010). The influence of aerosol particle number and hygroscopicity on the evolution of convective cloud systems and their precipitation: A numerical study based on the COPS observations on 12 August 2007. *Atmospheric Research*, *98*(1), 40-56. https://doi.org/10.1016/j.atmosres.2010.05.003

Prat, O. P., & Barros, A. P. (2007). A Robust Numerical Solution of the Stochastic Collection–Breakup Equation for Warm Rain. *Journal of Applied Meteorology and Climatology*, *46*(9), 1480-1497. https://doi.org/10.1175/JAM2544.1

Prat, O. P., Barros, A. P., & Williams, C. R. (2008). An Intercomparison of Model Simulations and VPR Estimates of the Vertical Structure of Warm Stratiform Rainfall during TWP-ICE. *Journal of Applied Meteorology and Climatology*, *47*(11), 2797-2815. https://doi.org/10.1175/2008JAMC1801.1

Pruppacher, H. R., & Klett, J. D. (1997). Microphysics of Clouds and precipitation. *Kluwer Academic, 954 pp*.

Raupach, T. H., & Berne, A. (2015). Correction of raindrop size distributions measured by Parsivel disdrometers, using a two-dimensional video disdrometer as a reference. *Atmospheric Measurement Techniques*, *8*(1), 343-365. https://doi.org/10.5194/amt-8-343-2015

Saleeby, S. M., Dolan, B., Bukowski, J., Van Valkenburg, K., van den Heever, S. C., & Rutledge, S. A. (2022). Assessing Raindrop Breakup Parameterizations Using Disdrometer Observations. *Journal of the Atmospheric Sciences*, *79*(11), 2949-2963. https://doi.org/10.1175/JAS-D-21-0335.1

Sant, V., Lohmann, U., & Seifert, A. (2013). Performance of a Triclass Parameterization for the Collision–Coalescence Process in Shallow Clouds. *Journal of the Atmospheric Sciences*, *70*(6), 1744-1767. https://doi.org/10.1175/JAS-D-12-0154.1

Seesselberg, M., Trautmann, T., & Thorn, M. (1996). Stochastic simulations as a benchmark for mathematical methods solving the coalescence equation. *Atmospheric research*, *40*(1), 33-48. https://doi.org/10.1016/0169-8095(95)00024-0

Seifert, A. (2002). Parametrisierung wolkenmikrophysikalischer Prozesse und Simulation konvektiver Mischwolken. Ph.D. Thesis, Institut für Meteorologie und Klimaforschung,
Universität Karlsruhe Forschungszentrum Karlsruhe, Karlsruhe (in German)

Seifert, A. (2008). On the Parameterization of Evaporation of Raindrops as Simulated by a One-Dimensional Rainshaft Model. *Journal of the Atmospheric Sciences*, *65*(11), 3608-3619. https://doi.org/10.1175/2008JAS2586.1

Seifert, A., & Beheng, K. D. (2001). A double-moment parameterization for simulating autoconversion, accretion and selfcollection. *Atmospheric research*, *59*, 265-281. https://doi.org/10.1016/S0169-8095(01)00126-0

Seifert, A., & Beheng, K. D. (2006). A two-moment cloud microphysics parameterization for mixed-phase clouds. Part 1: Model description. *Meteorology and atmospheric physics*, *92*(1-2), 45-66. https://doi.org/10.1007/s00703-005-0112-4

Seifert, A., Khain, A., Blahak, U., & Beheng, K. D. (2005). Possible Effects of Collisional Breakup on Mixed-Phase Deep Convection Simulated by a Spectral (Bin) Cloud Model. *Journal of the Atmospheric Sciences*, *62*(6), 1917-1931. https://doi.org/10.1175/JAS3432.1

Skamarock, W. C., Klemp, J. B., Dudhia, J., Gill, D. O., Barker, D. M., Duda, M. G., ... & Powers, J. G. (2008). A description of the advanced research WRF version 3. *NCAR technical note*, *475*, 113. https://doi.org/10.5065/D68S4MVH

Srivastava, R. C. (1978). Parameterization of Raindrop Size Distributions. *Journal of Atmospheric Sciences*, *35*(1), 108-117. https://doi.org/10.1175/1520-0469(1978)035<0108:PORSD>2.0.CO;2

Szakáll, M., & Urbich, I. (2018). Wind tunnel study on the size distribution of droplets after collision induced breakup of levitating water drops. *Atmospheric Research*, *213*, 51-56. https://doi.org/10.1016/j.atmosres.2018.05.007

Testud, J., Oury, S., Black, R. A., Amayenc, P., & Dou, X. (2001). The Concept of "Normalized" Distribution to Describe Raindrop Spectra: A Tool for Cloud Physics and Cloud Remote Sensing. *Journal of Applied Meteorology*, *40*(6), 1118-1140. https://doi.org/10.1175/1520-0450(2001)040<1118:TCONDT>2.0.CO;2

Tridon, F., & Battaglia, A. (2015). Dual-frequency radar Doppler spectral retrieval of rain drop size distributions and entangled dynamics variables. *Journal of Geophysical Research: Atmospheres*, *120*(11), 5585-5601. https://doi.org/10.1002/2014JD023023

Tridon, F., Battaglia, A., Chase, R. J., Turk, F. J., Leinonen, J., Kneifel, S., ... & Nesbitt, S. W. (2019a). The microphysics of stratiform precipitation during OLYMPEX: Compatibility between triple-frequency radar and airborne in situ observations. *Journal of Geophysical Research: Atmospheres*, *124*(15), 8764-8792. https://doi.org/10.1029/2018JD029858

Tridon, F., Battaglia, A., & Kollias, P. (2013a). Disentangling Mie and attenuation effects in rain using a Ka-W dual-wavelength Doppler spectral ratio technique. *Geophysical Research Letters*, *40*(20), 5548-5552. https://doi.org/10.1002/2013GL057454

Tridon, F., Battaglia, A., Kollias, P., Luke, E., & Williams, C. R. (2013b). Signal Postprocessing and Reflectivity Calibration of the Atmospheric Radiation Measurement Program 915-MHz Wind Profilers. *Journal of Atmospheric and Oceanic Technology*, *30*(6), 1038-1054. https://doi.org/10.1175/JTECH-D-12-00146.1

Tridon, F., Battaglia, A., Luke, E., & Kollias, P. (2017a). Rain retrieval from dual-frequency radar Doppler spectra: Validation and potential for a midlatitude precipitating case-study. *Quarterly Journal of the Royal Meteorological Society*, *143*(704), 1364-1380. https://doi.org/10.1002/qj.3010

Tridon, F., Battaglia, A., & Watters, D. (2017b). Evaporation in action sensed by multiwavelength Doppler radars. *Journal of Geophysical Research: Atmospheres*, *122*(17), 9379-9390. https://doi.org/10.1002/2016JD025998

Tridon, F., Planche, C., Mroz, K., Banson, S., Battaglia, A., Van Baelen, J., & Wobrock, W. (2019b). On the Realism of the Rain Microphysics Representation of a Squall Line in the WRF Model. Part I: Evaluation with Multifrequency Cloud Radar Doppler Spectra Observations. *Monthly Weather Review*, *147*(8), 2787-2810. https://doi.org/10.1175/MWR-D-18-0018.1

Tridon, F., Silber, I., Battaglia, A., Kneifel, S., Fridlind, A., Kalogeras, P., & Dhillon, R. (2022). Highly supercooled riming and unusual triple-frequency radar signatures over McMurdo Station, Antarctica. *Atmospheric Chemistry and Physics*, *22*(18), 12467-12491. https://doi.org/10.5194/acp-22-12467-2022

Tzivion (Tzitzvashvili), S., Feingold, G., & Levin, Z. (1987). An Efficient Numerical Solution to the Stochastic Collection Equation. *Journal of Atmospheric Sciences*, *44*(21), 3139-3149. https://doi.org/10.1175/1520-0469(1987)044<3139:AENSTT>2.0.CO;2

Van Weverberg, K., Vogelmann, A. M., Morrison, H., & Milbrandt, J. A. (2012). Sensitivity of Idealized Squall-Line Simulations to the Level of Complexity Used in Two-Moment Bulk Microphysics Schemes. *Monthly Weather Review*, *140*(6), 1883-1907. https://doi.org/10.1175/MWR-D-11-00120.1

Verlinde, J., & Cotton, W. R. (1993). Fitting Microphysical Observations of Nonsteady Convective Clouds to a Numerical Model: An Application of the Adjoint Technique of Data Assimilation to a Kinematic Model. *Monthly Weather Review*, *121*(10), 2776-2793. https://doi.org/10.1175/1520-0493(1993)121<2776:FMOONC>2.0.CO;2

Wacker, U., & Seifert, A. (2001). Evolution of rain water profiles resulting from pure sedimentation: Spectral vs. parameterized description. *Atmospheric research*, *58*(1), 19-39. https://doi.org/10.1016/S0169-8095(01)00081-3

Wan, H., Giorgetta, M. A., Zängl, G., Restelli, M., Majewski, D., Bonaventura, L., ... & Förstner, J. (2013). The ICON-1.2 hydrostatic atmospheric dynamical core on triangular grids–Part 1: Formulation and performance of the baseline version. *Geoscientific Model Development*, *6*(3), 735-763. https://doi.org/10.5194/gmd-6-735-2013

Williams, C. R., Bringi, V. N., Carey, L. D., Chandrasekar, V., Gatlin, P. N., Haddad, Z. S., Meneghini, R., Joseph Munchak, S., Nesbitt, S. W., Petersen, W. A., Tanelli, S., Tokay, A., Wilson, A., & Wolff, D. B. (2014). Describing the Shape of Raindrop Size Distributions Using Uncorrelated Raindrop Mass Spectrum Parameters. *Journal of Applied Meteorology and Climatology*, *53*(5), 1282-1296. https://doi.org/10.1175/JAMC-D-13-076.1

Wood, R. (2006). Rate of loss of cloud droplets by coalescence in warm clouds, *J. Geophys. Res.*, *111*, D21205. https://doi.org/10.1029/2006JD007553

Ziegler, C. L. (1984). Retrieval of thermal ad microphysical variables in observed convective storms. Ph.D. dissertation, University of Oklahoma, 196 pp.

Ziegler, C. L. (1985). Retrieval of Thermal and Microphysical Variables in Observed Convective Storms. Part 1: Model Development and Preliminary Testing. *Journal of Atmospheric Sciences*, *42*(14), 1487-1509. https://doi.org/10.1175/1520-0469(1985)042<1487:ROTAMV>2.0.CO;2

Ziemer, C., & Wacker, U. (2012). Parameterization of the Sedimentation of Raindrops with Finite Maximum Diameter. *Monthly Weather Review*, *140*(5), 1589-1602. https://doi.org/10.1175/MWR-D-11-00020.1

Supporting Information for

Evaluation of the representation of raindrop self-collection and breakup in two-moment bulk models using a multifrequency radar retrieval

Laurence Niquet[1], Frédéric Tridon[2,1], Pierre Grzegorczyk[1], Antoine Causse[1], Baptiste Bordet[3], Wolfram Wobrock[1], and Céline Planche[1,4]

[1]Université Clermont Auvergne, CNRS INSU, Laboratoire de Météorologie Physique UMR 6016, F-63000 Clermont-Ferrand, France.

[2]DIATI, Politecnico di Torino, Turin, Italy.

[3]Université Grenoble Alpes, Laboratoire Interdisciplinaire de physique UMR 5588, F-38000 Grenoble, France.

[4]Institut Universitaire de France (IUF).

Corresponding authors: Céline Planche (celine.planche@uca.fr) and Frédéric Tridon (frederic.tridon@polito.it)

Supplementary

Time-height evolution of the parameters retrieved by the multifrequency radar technique

As mentioned in Section 3 of the main document, from the RSD profiles obtained by the multifrequency radar retrieval of Tridon and Battaglia (2015), it is possible to determine the profiles of microphysical parameters used in our study. Figures S1 and S2 show the time-height evolution of the mean volume diameter D_{mv}, the total raindrop concentration N_r, the rain water content RWC and the vertical wind speed w for the Finland case (Figure S1) and Oklahoma case (Figure S2). The vertical dashed lines in Figure S1 represent the period studied for the Finland case. In Figure S2, the three periods (CR, TZ and SR) of the squall line observed in Oklahoma (see Section 3 of the main document) are delimited by vertical dashed lines. For this case, the period studied in our work is the combination of TZ and SR. These figures show that the precipitating layer in the Finland case is less homogeneous than in the Oklahoma case. Indeed, several zones of distinct N_r, D_{mv} and RWC trends are visible in Figures S1b-d. Our analysis is focused on the period where the RWC is sufficiently large that the corresponding Ka-W differential attenuation is significant, a condition for providing accurate estimates of RWC and raindrop concentration (Tridon et al., 2017a). This period is marked by a slight wind ascendance (Figure S1e). A decrease in total raindrop concentration N_r associated to an increase in mean volume diameter D_{mv} towards the ground is visible for the Finland case (Figures S1b-c) but it is less marked than for the Oklahoma case (Figures S2b-c) (as also described in the statistical analysis shown in Figure 5 of the main document). For the Oklahoma case, we observe smaller D_{mv} and lower N_r in the TZ compared to the SR (as already reported in Tridon et al., 2019b and Planche et al., 2019). Also, contrary to the Finland case, quite intense downdrafts are predominantly visible in TZ and SR

(Figures S2e), an interesting contrast between the cases which could translate in different RSD variability (as discussed in Section 3 of the main document). In the end, by considering properly the impact of the vertical wind in the calculation of the trajectories of the raindrops (Section 4 of the main document), we obtain a very similar behavior for the two cases, which shows that, as expected, the parameterization of the self-collection and breakup processes is invariable to the vertical wind.

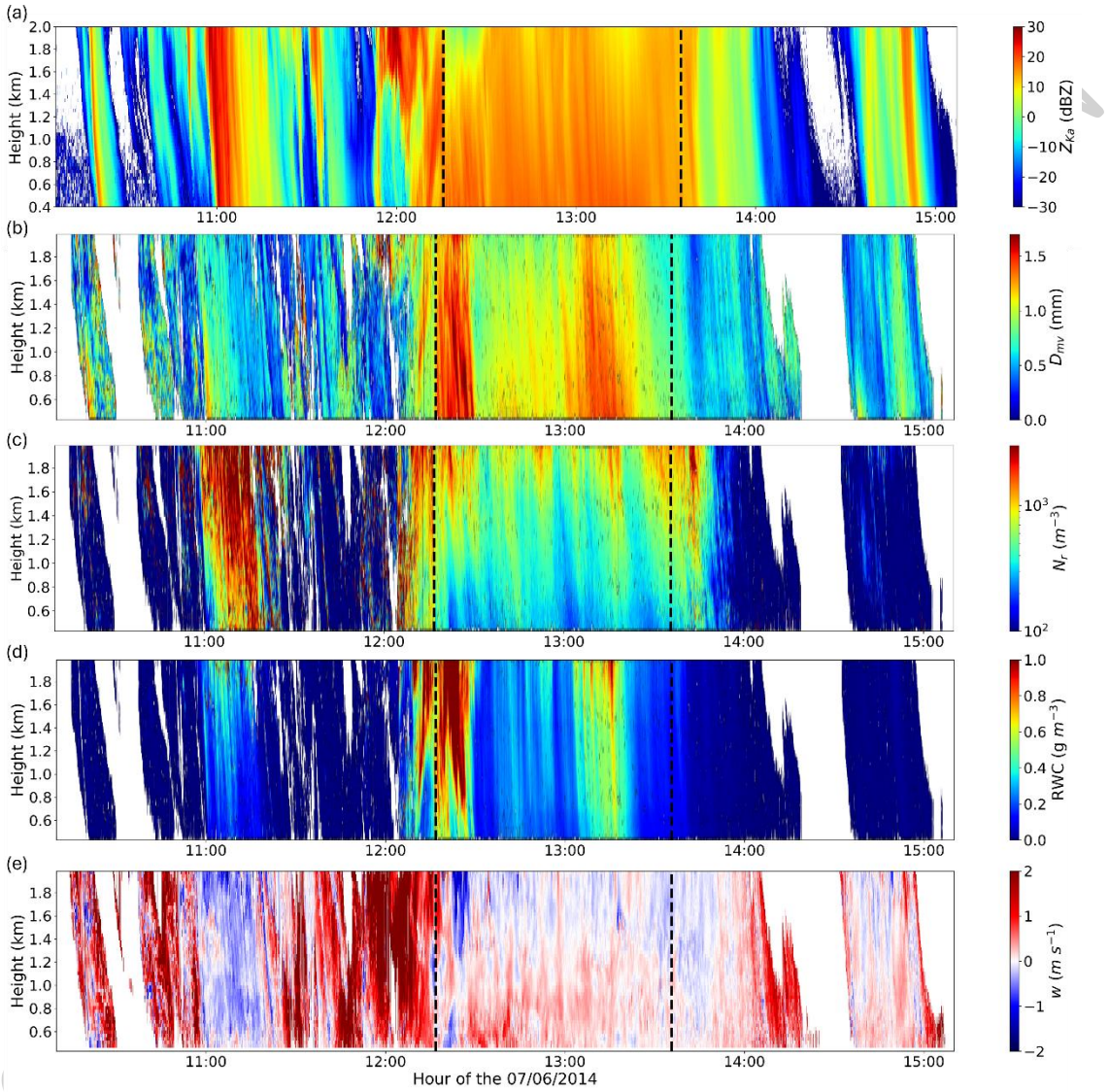

Figure S1. Time-height evolution of the ARM K_a-band radar reflectivity (KAZR) (a) and the retrieved parameters for the Finland case: (b) mean volume diameter D_{mv}, (c) total raindrop concentration N_r, (d) rain water content RWC and (e) vertical wind speed w. The vertical dashed lines represent the period studied. The x axis label corresponds to the hour of the dd/mm/yyyy.

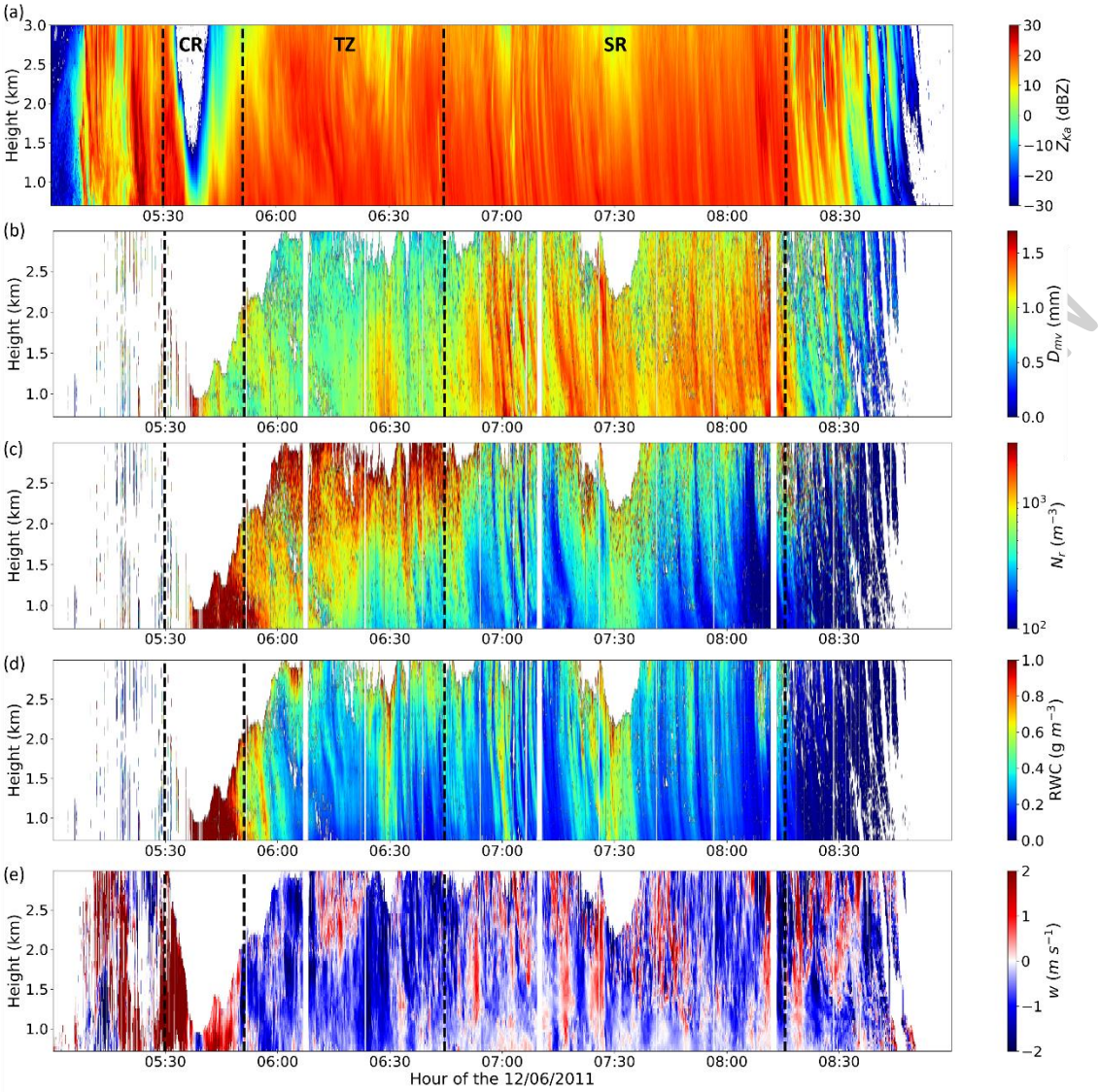

Figure S2. Time-height evolution of the ARM K_a-band radar reflectivity (KAZR) (a) and the retrieved parameters for Oklahoma case: (b) mean volume diameter D_{mv}, (c) total raindrop concentration N_r, (d) rain water content RWC and (e) vertical wind speed w. The vertical dashed lines represent the three periods (CR: Convective Region, TZ: Transition Zone, and SR: Stratiform Region) of the squall line defined in Section 3 of the main document. The x axis label corresponds to the hour of the dd/mm/yyyy.

Results for individual cases

The results shown in Section 5 of the main document for the two cases together were also carried out for each case individually. Figure S3 represents the same variables as in Figures 8, 9 and 10 of the main document but only for the Finland case (a, c, e) and for the Oklahoma case (b, d, f). These figures suggest that there is enough data in each case to carry out our study and derive a fit for each case. These two cases complement each other in terms of size ranges, as shown in Figures S3a-b and S3e-f, there is more data for small diameters for the Oklahoma than for the Finland case. It is also visible for the rain self-collection efficiency (Figures S3c-d), where the

large amount of D_{mv} points around 1.25 mm of the Oklahoma case completes the data from the Finland case. The final parameterization diverges between the two cases only for the largest diameters (D_{mv} > 1.5 mm^3), suggesting that our parameterization is slightly more uncertain for this range of D_{mv} which are not the most frequently observed. In addition, we observe a bit more extreme points in the Oklahoma case than in the Finland case, but the overall variability is similar for both cases and can be explained by uncertainty of the radar retrieval, as shown by the gray error bars. Note that the color scale is adjusted for each case, and that there are more data for the Finland case.

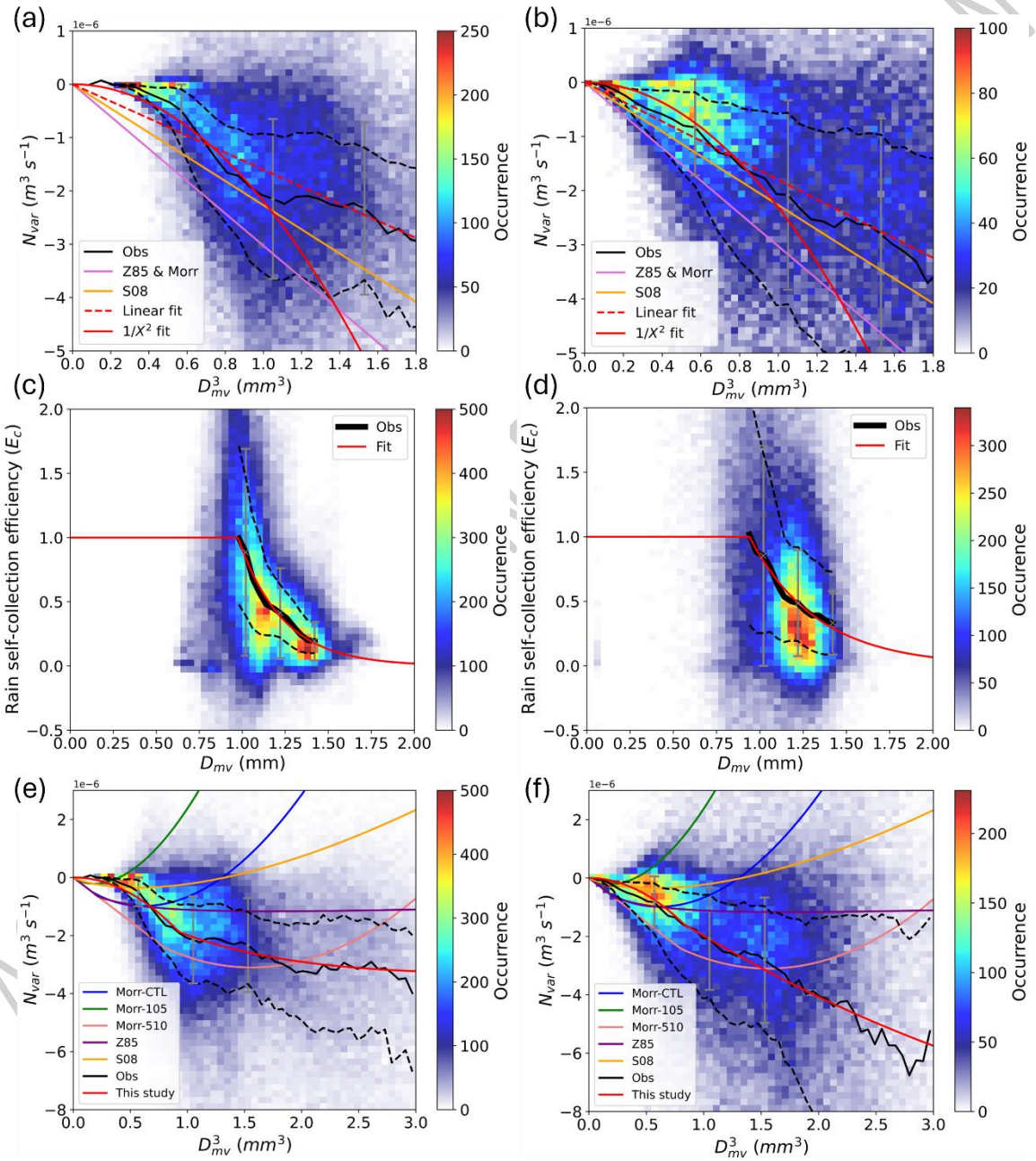

Figure S3. Probability density function of $N_{\mathrm{var}} = (1/N_{\mathrm{r}}^2)(dN_{\mathrm{r}}/dt)$ as a function of D^3_{mv} (a, b and e, f) and probability density function of the rain self-collection efficiency (E_{c}) as a function of D_{mv} (c, d) with observation points corresponding to the Finland case (a, c, e) and the Oklahoma case (b, d, f) shown as a density plot in color. The median of the observations per bin of diameter is represented by the black solid line and the first (Q1) and third (Q3) quartiles

are represented by the black dashed lines. The error bars in gray represent the uncertainty of the retrieval for a single radar pixel. In (a) and (b) are shown the parameterizations of the self-collection process only (i.e. with E_c parameter set equal to 1) of Ziegler (1985) and Morrison et al. (2012) (Z85 & Morr) in purple and of Seifert (2008) (S08) in orange. The linear fit of the median of observations is shown by the red dashed line and the fit in $1/X^2$ (i.e. the final parameterization) by the continuous red line. In (c) and (d), the exponential fit of the median of observations is shown by the red solid line. In (e) and (f) are shown the parameterizations of the self-collection and breakup processes of Ziegler (1985) (Z85), of Morrison et al. (2012) (Morr-CTL, Morr-105 and Morr-510) and Seifert (2008) (S08) by the purple, blue, green, pink and orange lines, respectively. The parameterization adapted to each case is represented in red.

References

Morrison, H., Tessendorf, S. A., Ikeda, K., & Thompson, G. (2012). Sensitivity of a Simulated Midlatitude Squall Line to Parameterization of Raindrop Breakup. *Monthly Weather Review*, *140*(8), 2437-2460. https://doi.org/10.1175/MWR-D-11-00283.1

Planche, C., Tridon, F., Banson, S., Thompson, G., Monier, M., Battaglia, A., & Wobrock, W. (2019). On the Realism of the Rain Microphysics Representation of a Squall Line in the WRF Model. Part II: Sensitivity Studies on the Rain Drop Size Distributions. *Monthly Weather Review*, *147*(8), 2811-2825. https://doi.org/10.1175/MWR-D-18-0019.1

Seifert, A. (2008). On the Parameterization of Evaporation of Raindrops as Simulated by a One-Dimensional Rainshaft Model. *Journal of the Atmospheric Sciences*, *65*(11), 3608-3619. https://doi.org/10.1175/2008JAS2586.1

Tridon, F., & Battaglia, A. (2015). Dual-frequency radar Doppler spectral retrieval of rain drop size distributions and entangled dynamics variables. *Journal of Geophysical Research: Atmospheres*, *120*(11), 5585-5601. https://doi.org/10.1002/2014JD023023

Tridon, F., Battaglia, A., Luke, E., & Kollias, P. (2017a). Rain retrieval from dual-frequency radar Doppler spectra: Validation and potential for a midlatitude precipitating case-study. *Quarterly Journal of the Royal Meteorological Society*, *143*(704), 1364-1380. https://doi.org/10.1002/qj.3010

Tridon, F., Planche, C., Mroz, K., Banson, S., Battaglia, A., Van Baelen, J., & Wobrock, W. (2019b). On the Realism of the Rain Microphysics Representation of a Squall Line in the WRF Model. Part I: Evaluation with Multifrequency Cloud Radar Doppler Spectra Observations. *Monthly Weather Review*, *147*(8), 2787-2810. https://doi.org/10.1175/MWR-D-18-0018.1

Ziegler, C. L. (1985). Retrieval of Thermal and Microphysical Variables in Observed Convective Storms. Part 1: Model Development and Preliminary Testing. *Journal of Atmospheric Sciences*, *42*(14), 1487-1509. https://doi.org/10.1175/1520-0469(1985)042<1487:ROTAMV>2.0.CO;2